

**Special Section:**

The Mars Perseverance Rover  
Jezero Crater Floor Campaign

D. Toledo and V. Apéstigue contributed  
equally to this work.

**Key Points:**

- A dust devil frequency of occurrence of between 1.3 and 3.4 dust devils  $\text{km}^{-2} \text{sol}^{-1}$  was derived from MEDA-RDS observations for the first 365 sols, displaying the maximum activity at around noon and increasing as we move from spring into summer
- We find an average dust devil diameter of 29 m (or a median diameter of 25 m) and maximum and minimum diameters of  $132 \pm 63.4$  m and  $5.6 \pm 5.5$  m
- Dust devil migration directions are in agreement with the MEDA background wind direction measurements

**Supporting Information:**

Supporting Information may be found in  
the online version of this article.

**Correspondence to:**

D. Toledo,  
toledocd@inta.es

**Citation:**

Toledo, D., Apéstigue, V., Arruego, I., Lemmon, M., Gómez, L., Montoro, F., et al. (2023). Dust devil frequency of occurrence and radiative effects at Jezero crater, Mars, as measured by MEDA Radiation and Dust Sensor (RDS). *Journal of Geophysical Research: Planets*, 128, e2022JE007494. <https://doi.org/10.1029/2022JE007494>


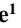


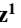






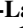

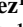



Received 20 JUL 2022

Accepted 4 JAN 2023

© 2023. The Authors.

This is an open access article under  
the terms of the [Creative Commons  
Attribution-NonCommercial-NoDerivs  
License](#), which permits use and  
distribution in any medium, provided the  
original work is properly cited, the use is  
non-commercial and no modifications or  
adaptations are made.

## Dust Devil Frequency of Occurrence and Radiative Effects at Jezero Crater, Mars, as Measured by MEDA Radiation and Dust Sensor (RDS)

D. Toledo<sup>1</sup> , V. Apéstigue<sup>1</sup> , I. Arruego<sup>1</sup> , M. Lemmon<sup>2</sup> , L. Gómez<sup>1</sup> , F. Montoro<sup>1</sup>,  
R. Hueso<sup>3</sup> , C. Newman<sup>4</sup> , M. Smith<sup>5</sup> , D. Viudez-Moreiras<sup>6</sup> , G. Martínez<sup>7</sup>, R. Lorenz<sup>8</sup> ,  
A. Vicente-Retortillo<sup>6</sup> , A. Sanchez-Lavega<sup>3</sup> , M. de la Torre Juárez<sup>9</sup>, J. A. Rodríguez-Manfredi<sup>6</sup>,  
I. Carrasco<sup>1</sup>, M. Yela<sup>1</sup> , J. J. Jimenez<sup>1</sup> , E. García-Menendez<sup>1</sup>, S. Navarro<sup>6</sup>, F. J. Gomez-Elvira<sup>1</sup>,  
A.-M. Harri<sup>10</sup>, J. Polkko<sup>10</sup> , M. Hieta<sup>10</sup> , M. Genzer<sup>10</sup>, N. Murdoch<sup>11</sup> , and E. Sebastian<sup>6</sup>

<sup>1</sup>Instituto Nacional de Técnica Aeroespacial (INTA), Madrid, Spain, <sup>2</sup>Space Science Institute, Boulder, CO, USA,

<sup>3</sup>Universidad del País Vasco UPV/EHU, Bilbao, Spain, <sup>4</sup>Aeolis Research, Chandler, AZ, USA, <sup>5</sup>NASA Godard Space Flight

Center, Greenbelt, MD, USA, <sup>6</sup>Centro de Astrobiología (INTA-CSIC), Madrid, Spain, <sup>7</sup>Lunar and Planetary Institute,

Universities Space Research Association, Houston, TX, USA, <sup>8</sup>Johns Hopkins Applied Physics Laboratory, Laurel, MD,

USA, <sup>9</sup>Jet Propulsion Laboratory, California Institute of Technology, Pasadena, CA, USA, <sup>10</sup>Finnish Meteorological Institute,

Helsinki, Finland, <sup>11</sup>Institut Supérieur de l'Aéronautique et de l'Espace (ISAE-SUPAERO), Université de Toulouse, Toulouse, France

**Abstract** The Mars Environmental Dynamics Analyzer, onboard the Perseverance rover, is a meteorological station that is operating on Mars and includes, among other sensors, the radiometer Radiation and Dust Sensor (RDS). From RDS irradiance observations, a total of 374 dust devils (DDs) were detected for the first 365 sols of the mission ( $L_s = 6^\circ\text{--}182^\circ$ ), which along with wind and pressure measurements, we estimated a DD frequency of formation at Jezero between 1.3 and 3.4 DD  $\text{km}^{-2} \text{sol}^{-1}$  (increasing as we move from spring into summer). This frequency is found to be smaller than that estimated at the Spirit or Pathfinder landing sites but much greater than that derived at InSight landing site. The maximum in DD frequency occurs between 12:00 and 13:00 local true solar time, which is when the convective heat flux and lower planetary boundary layer IR heating are both predicted to peak in Jezero crater. DD diameter, minimum height, and trajectory were studied showing (a) an average diameter of 29 m (or a median of 25 m) and a maximum and minimum diameter of  $132 \pm 63.4$  and  $5.6 \pm 5.5$  m; (b) an average minimum DD height of 231 m and a maximum minimum-height of 872 m; and (c) the DD migration direction is in agreement with wind measurements. For all the cases, DDs decreased the UV irradiance, while at visible or near-IR wavelengths both increases and decreases were observed. Contrary to the frequency of formation, these results indicate similar DD characteristics in average for the studied period.

**Plain Language Summary** Dust devils are dry, dusty convective vortices that play a key role in the dust cycle on Mars by lifting dust from the surface to the atmosphere. Parameters like the dust devil formation frequency or size characteristics are key to constrain their contribution to the planet's dust budget. Using observations made by the Radiation and Dust Sensor of the instrument Mars Environmental Dynamics Analyzer onboard Perseverance rover, we estimated the dust devil (DD) frequency for the full diurnal cycle in Jezero crater, Mars, during the first half of the Martian year. We find that between 1 and 3 DD per  $\text{km}^{-2}$  form every day, mainly around noon, and they become more frequent as spring advances to summer. The formation frequency is smaller than that estimated at the Spirit landing site but much greater than the values derived at InSight landing site, indicating a high variability in activity depending on location. When the DDs blocked the direct sunlight from reaching the sensor, we estimated their diameters to range between 5 and 130 m with an average of 29 m. In all detections, the presence of DDs resulted in a decrease of the measured UV radiation.

### 1. Introduction

On Mars, the dust cycle is a critical factor that drives the weather and climate of the planet (Read & Lewis, 2004; Zurek et al., 1992). Airborne dust affects the absorption and scattering of the solar radiation, directly affecting the energy balance that drives the atmospheric dynamics of the planet. In turn, the atmospheric dynamics influences the distribution of the dust particles and the distribution of surface dust lifting (DL), thus setting up a

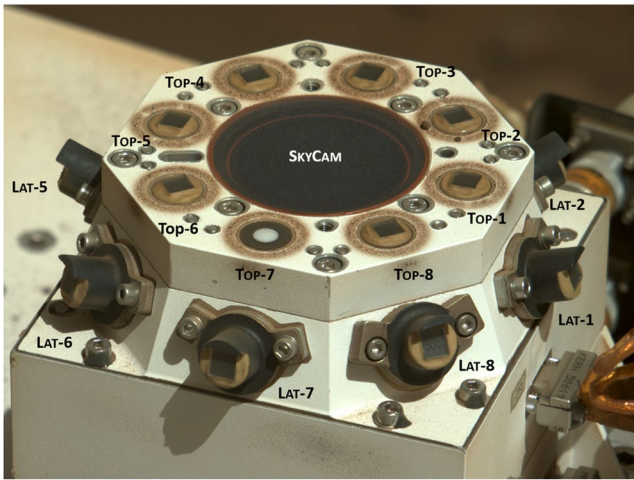
**Author Contributions:**

**Conceptualization:** D. Toledo, V. Apéstigue, I. Arruego  
**Data curation:** D. Toledo, V. Apéstigue, I. Arruego, M. Lemmon, L. Gómez, F. Montoro, R. Hueso, C. Newman, M. Smith, D. Viudez-Moreiras, G. Martínez, M. de la Torre Juárez, J. A. Rodríguez-Manfredi, J. J. Jimenez, E. García-Menendez, S. Navarro, F. J. Gomez-Elvira, A.-M. Harri, J. Polkko, M. Hieta, M. Genzer, N. Murdoch, E. Sebastian  
**Formal analysis:** D. Toledo, V. Apéstigue, I. Arruego  
**Funding acquisition:** I. Arruego, J. A. Rodríguez-Manfredi  
**Investigation:** D. Toledo, V. Apéstigue, I. Arruego  
**Methodology:** D. Toledo, V. Apéstigue, I. Arruego  
**Software:** D. Toledo, V. Apéstigue, I. Arruego, R. Hueso, I. Carrasco  
**Validation:** D. Toledo, V. Apéstigue, I. Arruego, I. Carrasco  
**Visualization:** D. Toledo, V. Apéstigue, I. Arruego, I. Carrasco  
**Writing – original draft:** D. Toledo, V. Apéstigue  
**Writing – review & editing:** D. Toledo, V. Apéstigue, I. Arruego, M. Lemmon, L. Gómez, R. Hueso, C. Newman, M. Smith, D. Viudez-Moreiras, G. Martínez, R. Lorenz, A. Vicente-Retortillo, A. Sanchez-Lavega, M. de la Torre Juárez, J. A. Rodríguez-Manfredi, M. Yela, J. J. Jimenez, N. Murdoch

complex feedback process. This type of nonlinear feedback mechanism is thought to be the cause of the observed year-to-year variability in the dust-storm activity (global, regional, and local scales). Therefore, for studying the present-day and recent-past climate of Mars we need to observe and understand the different processes involved in the dust cycle. To date, two main mechanisms have been identified for the lifting of the dust particles: lifting by dust devils (e.g., M. Balme & Greeley, 2006; Toigo et al., 2003) and by wind stress (e.g., Bagnold, 2012; Kok et al., 2012; Sullivan & Kok, 2017). In modeling studies, DD lifting has been suggested to account for about 50% of the total dust budget (e.g., Kahre et al., 2006), where the peak in such lifting occurs outside the dust storm season. However, in such large-scale models (grid spacing  $\sim 100$  s of km), the parameterization of DD lifting is also accounting for any subgrid scale (unresolved) lifting associated with smaller scale convective motions, which would include the lifting by convectively driven wind gusts that has also been observed in Jezero (C. E. Newman et al., 2022). Observations of DDs from orbit, although only sensitive to DDs above a certain size and with some other biases, provide another estimate of their contribution to the global dust budget and demonstrate that this is significant, especially through northern spring and summer when large dust storms are far less frequent (Cantor et al., 2006). For these reasons, DDs have been proposed as one of the main components in the Martian dust cycle and thus in the sustenance of the ever-observed dust haze layer (e.g., Fisher et al., 2005). Although a number of modeling groups have simulated aspects of the dust cycle with Mars global climate models (Basu et al., 2004; Haberle et al., 2003; C. E. Newman et al., 2002), no climate model completely reproduces the observed dust cycles and storms. Indeed, additional surveys of DD observations, along with measurements of DL by wind stress, are needed to place quantitative constraints on the diurnal cycles of these events. These surveys should include both surface and orbital observations, and the range of observations must encompass the full diurnal period and consider the wider meteorological context surrounding the observations.

Since the first observation of a DD on Mars from the Viking Orbiter (Thomas & Gierasch, 1985), many instruments on Mars have been used to identify and characterize DDs. Several cameras and imaging system onboard orbiters have provided DD images from which the size of the DD can be estimated (e.g., Cantor et al., 2006; Cushing et al., 2005; L. Fenton et al., 2016; Fisher et al., 2005; Reiss, Hoekzema, & Stenzel, 2014; Reiss, Spiga, & Erkeling, 2014; Stanzel et al., 2008; Thomas & Gierasch, 1985; Towner, 2009). Orbiters also provide images of the tracks produced by the DDs on the Martian surface (e.g., Cantor et al., 2006; Reiss et al., 2016; Wang et al., 2021; Whelley & Greeley, 2008), allowing the occurrence of these phenomena during a given time period and in specific regions of the planet to be estimated. These measurements, covering large geographic areas, have demonstrated that DDs can be found at a wide range of latitudes (from 0 to about 70° in both hemispheres) and at any longitudes on Mars. However, both kind of measurements are biased toward the largest DD sizes, since only the largest DDs are directly observed from orbiters, and only 10%–20% produce tracks on the surface (Cantor et al., 2006). In addition, most of the orbiters observe the same geographical location at a similar local time each Sol. Thus, daily temporal variation of the DDs is difficult to obtain from most of these data sets. The moment at which DDs are produced is even more difficult to determine when studying DD tracks since the tracks can persist for whole seasons (M. R. Balme et al., 2003; Daubar et al., 2018). Cameras and imagers on landers and rovers of several missions have also captured DD images (e.g., Ferri et al., 2003; Greeley et al., 2006; Metzger, 1999; Metzger et al., 2000; Moores et al., 2015). Variations of some meteorological variables such as wind speed, wind direction, temperature or pressure, recorded also from Mars landers and rovers, have been studied to characterize vortices, which may be clear or dusty (DDs), and to estimate their occurrence (e.g., Ellehoj et al., 2010; Ferri et al., 2003; Greeley et al., 2003; Kahanpää & Viúdez-Moreiras, 2021; Kahanpää et al., 2016; R. D. Lorenz, 2016; Murphy & Nelli, 2002; C. E. Newman et al., 2019; Ordonez-Etxeberria et al., 2018; Steakley & Murphy, 2016). Despite providing very valuable information, images are usually constrained by the field of view (FOV) of the camera and the typically very short time period over which such imaging is possible, while events inferred from meteorological variables such as pressure may correspond to clear rather than dusty vortices (DDs), in the absence of additional evidence. This is why orbiter (global picture of the phenomena) and lander (more sensitive to the lowest atmospheric layers and to smaller DD) data are complementary.

To provide a complete meteorological context of the observations, the Mars Environmental Dynamics Analyser (MEDA) station (Rodríguez-Manfredi et al., 2021), onboard of the Mars 2020 rover Perseverance (Farley et al., 2020), includes a set of sensors capable of measuring the radiance fluxes over the Martian surface. Combining these observations with radiative transfer (RT) simulations, airborne dust particles can be detected and characterized (optical depth, particle size, and refractive index) over the day with high temporal resolution (Toledo et al., 2017). The great azimuthal range covered by the FOV of MEDA's different photodetectors (including



**Figure 1.** Image of RDS showing the disposition of the upper (top) and lateral (Lat) detectors and SkyCam. Credits JPL/Caltech.

the MEDA's Skycam camera) provides a global picture of the surroundings of the rover. Combining data from different MEDA sensors, we are able to discriminate DDs from other DL events (such as DL by wind gusts) or establish when a particular vortex is lifting dust.

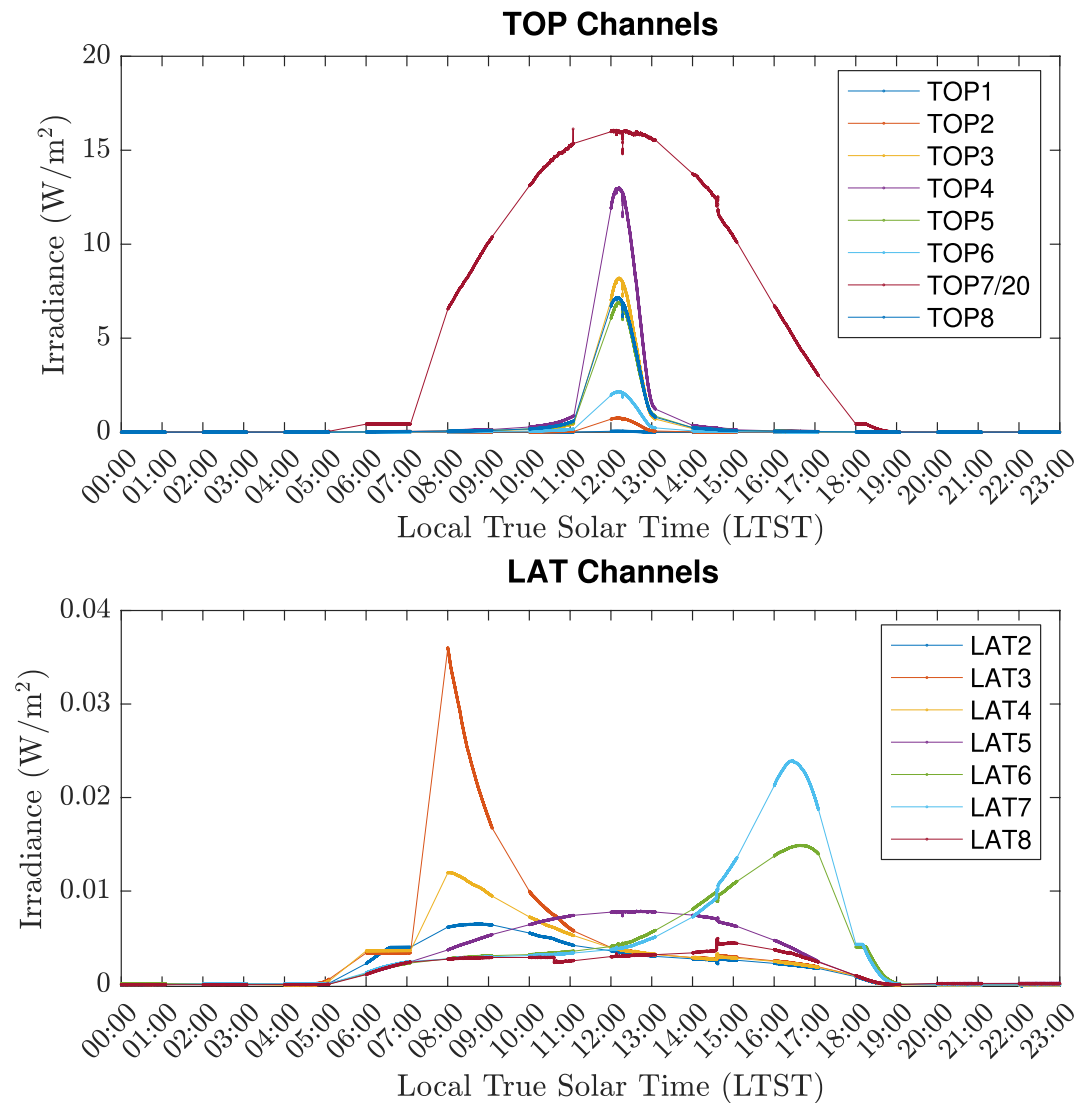
In this work, we analyzed observations acquired by MEDA, in particular by the Radiation and Dust sensor (RDS), during the first 365 sols to constrain the DD frequency of formation at Jezero crater, as well as to derive DD properties such as DD diameter, trajectory, or advection velocity. In order to better constrain the DD properties, the observations were analyzed with RT simulations and combined with measurements made by other MEDA sensors (e.g., pressure). We describe the data used in this work, the RT model, the principle of detection, and simultaneous detections with other instruments in Section 2. In Section 3, we present our model results, compare them to data, and discuss the impact of our results.

## 2. Methodology

### 2.1. RDS Measurements

The MEDA instrument (Rodriguez-Manfredi et al., 2021) is a meteorological station onboard the Perseverance rover with the aim of characterizing the daily and seasonal evolution of the Jezero crater environment. The instrument includes two wind sensors (WS) to infer wind direction and speed, five thermal sensors at different locations and heights (ATS), an infrared radiometer (TIRS) to measure the downward and upward LW and upward SW radiation at the surface and also provides the ground and  $\sim 40$  m altitude temperatures, a relative humidity sensor, a pressure sensor (PS), and the ultraviolet A (UVA) to near infrared radiometer RDS dedicated to studying dust and clouds (Apestigue et al., 2022). RDS takes its heritage from previous Mars developments (Arruego et al., 2017; Gómez-Elvira et al., 2012) and is comprised of two sets of photodetectors (RDS-DP) and a camera pointing at zenith (RDS-SkyCam). The first set of photodetectors, the Top channels, corresponds to eight zenith-pointed detectors, which cover the light spectrum from UVA to Near IR (Top-1 to Top-8: 255, 259, 250–400, 450, 650, 750, 190–1,100, and 950 nm). Most of the Top detectors use interferential filters and mechanical masks to constrain their FoV (FoV) to  $\pm 15^\circ$  zenith angle, while the Top-7 channel covers the full sky from  $0^\circ$  to  $90^\circ$  zenith angle and for all azimuth angles. These channels have strong surrounding magnets to minimize the dust deposited over the sensors (Gómez-Elvira et al., 2012). The second set corresponds to the eight Lateral (Lat) channels, which are pointed sideways at  $20^\circ$  above the rover deck (except Lat-8, which is  $35^\circ$ ) and with  $45^\circ$  degrees in azimuth between them. Lateral channels are all centered at the same wavelength (750 nm) and have a FoV of  $\pm 5^\circ$  (see Figures 1 and 2). The Lat-1 is blinded and serves as a monitor of the possible photodetectors degradation due to the radiation accumulated during the mission. RDS-DP is able to operate at 1 Hz during MEDA sessions of measurements, which often cover around 12 hr per sol.

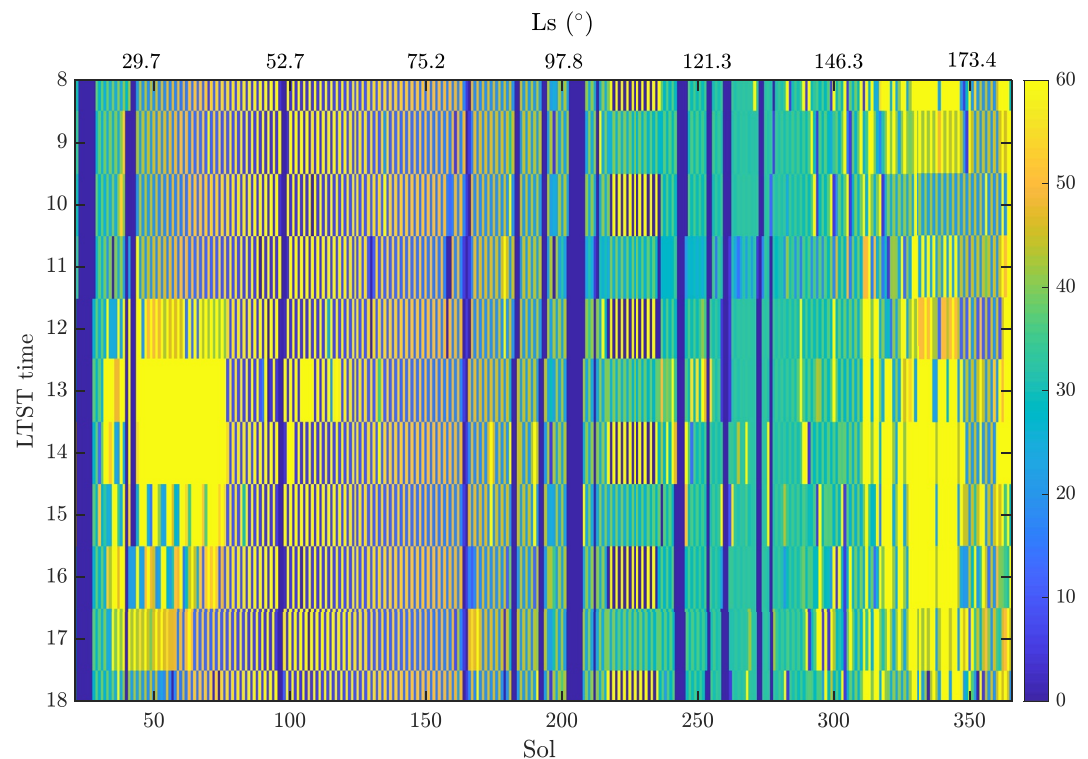
The camera, SkyCam, takes its heritage from the engineering cameras of the Mars Exploration Rover and Mars Science Laboratory missions (J. Maki et al., 2003, 2012). The electronics remain the same but the optics have been redesigned to be able to take pictures of the sky. The outermost Skycam lens has an annular coating of semiopaque material. When the sun is in such a position that it sits behind this annulus (at most times of the year, this occurs twice per day, in the morning and afternoon) an image is taken and used to derive the atmospheric opacity. The combination of these two sensing technologies allows RDS to characterize the optical and scattering properties of suspended dust, detect and characterize clouds during twilight, estimate the ozone column abundance from the Martian surface (from UV channels), and detect DL events such as DDs at a high sampling frequency and for long periods of time. In general, MEDA sampling is set at 1 Hz with all sensors operating for blocks of  $\sim 1$  hr. The disposition of the blocks along the day are selected for each sol based on the atmospheric research activities, and the duration and number of block sometimes change depending on power availability and data volume constrains. Figure 3 shows the hours covered by MEDA for the first 365 sols, and demonstrates good coverage of the most convective period ( $\sim 08:00$  through  $17:00$ ) when DD activity is at its peak (see Section 3.2). As we will see in the following section, the MEDA time coverage is key for estimating the DD frequency of formation.



**Figure 2.** Example of RDS signals measured by RDS Top (top panel) and Lat sensors (lower panel) on sol 128. For representing purposes, the Top-7 signal was divided by a factor of 20. The maximum of Top sensors (those pointing at zenith) signals occurs when the sun is at the minimum solar zenith angle. However, for Lat sensors a significant increase only occurs when the sun is low and near to the sensor-azimuth-pointing direction (in this example Lat-3 in the morning, and Lat-6 and Lat-7 in the evening).

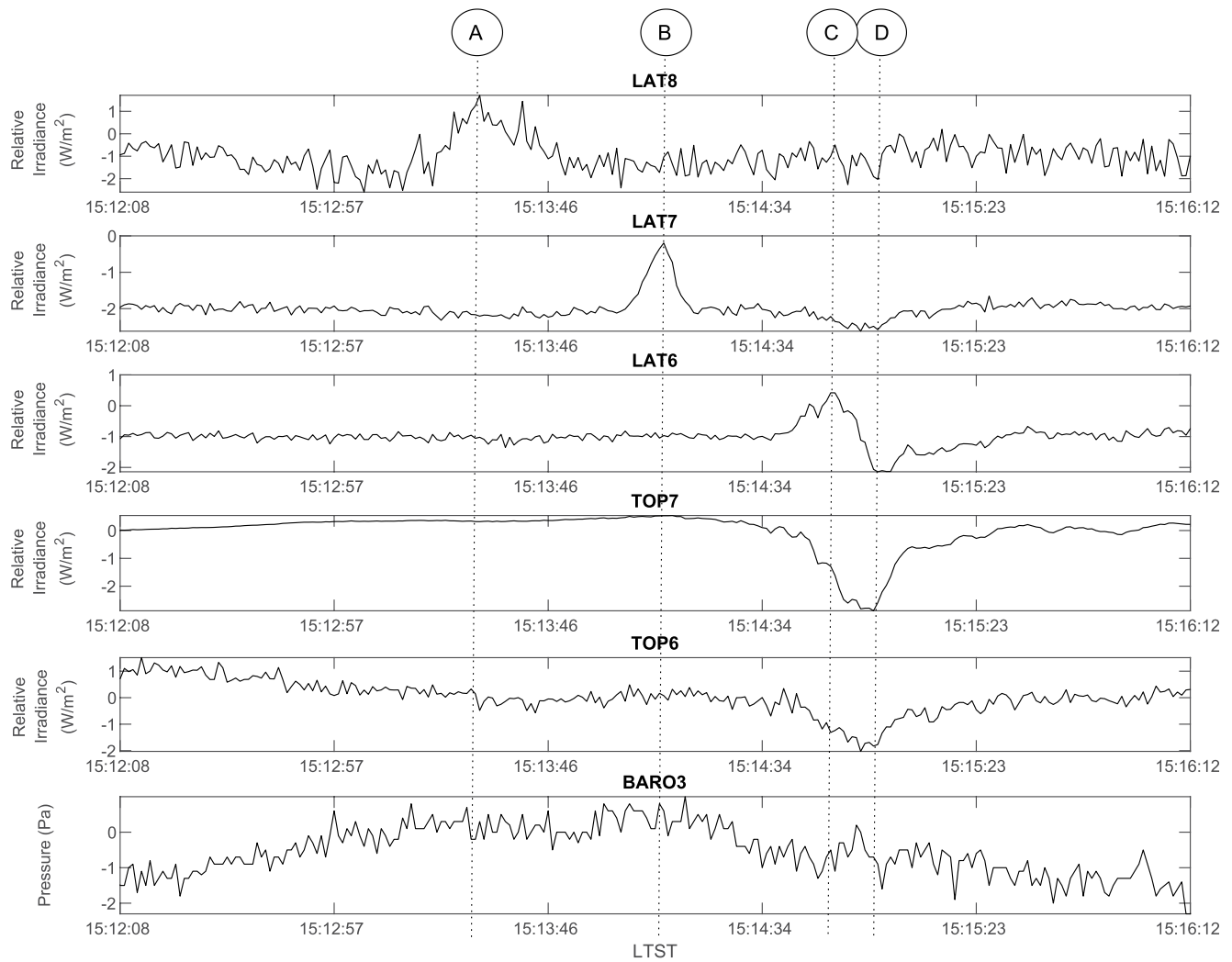
## 2.2. Dust Lifting Detection With RDS

The approach used to detect and characterize DDs using RDS observations is based on the expected changes in sky brightness when a DD is near the rover. If the DD crosses the FOV of one sensor, then a change in the signal intensity is expected (note that each sensor measures the solar irradiance weighted by its FOV). The variations caused by the DD can be positive or negative (as observed in terrestrial analog observations, e.g., R. D. Lorenz and Jackson (2015), and in observations of solar array currents on the InSight lander, R. D. Lorenz et al. (2021)), depending on the DD properties and position, the spectral band and orientation of the sensor, and the solar zenith (SZA) and azimuth (PHI0) angles. Figure 4 shows a sequence of signal variations produced by the first DD detected by RDS. In order to enhance the DD signature, the background signals, obtained by fitting the data just before and after the detection to a polynomial function, were subtracted from the observations (see Section 3.1 for a complete description of the procedure employed to detect DD in RDS signals). This detection occurred on sol 21 at 15:13:30 local true solar time (LTST). The data acquired by the PS during this event is also shown in Figure 4 (bottom panel). The first detection was made by the Lat-8 sensor (circle A in

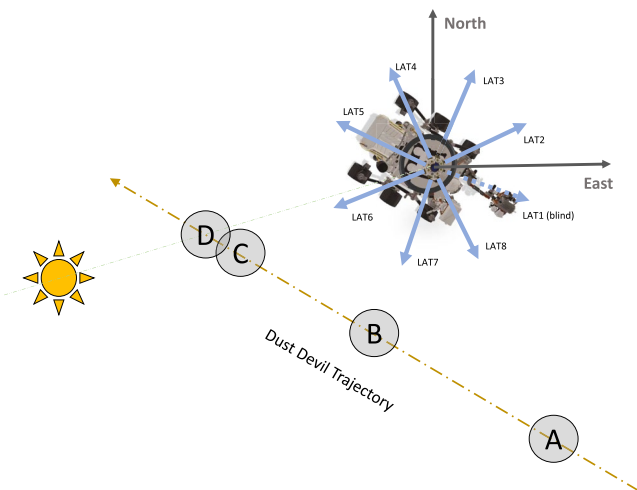


**Figure 3.** Day-time MEDA temporal coverage during the first 365 sols of the mission (colorbar units in minutes).

Figure 4) which displayed, as a result of the dust scattering, an increase of about 1.1%. Subsequently, the DD crossed the Lat-7 FOV (signal variation indicated with circle B in Figure 4) about 43 s after the Lat-8 detection, increasing by 1.3% the irradiance measured by the sensor. The last lateral detection was performed by the Lat-6 sensor 40 s later and consisted of an intensity increase of 0.28% (circle C in Figure 4). Just after the increase in the Lat-6 signal, which is due to an increase in scattered light, a decrease occurs in the same signal which is caused by the blocking of direct light; in this particular moment the DD is located between the Lat-6 sensor and the sun. This direct light-blocking is also found in the Top sensor measurements, where we see a minimum in the signals  $\sim 9$  s after the last lateral detection (see circle D in Figure 4). Following the detections sequence described above, Figure 5 shows the rover and RDS sensor orientations during this event, the sun position ( $263^\circ$  with respect to North clockwise), and the possible trajectory of the DD. The information about the rover position and orientation as well as the sun location was obtained from the ancillary data of M2020 (also available at NASA's Planetary Data System). The rover Yaw angle measured from North was  $127.84^\circ$ , hence the RDS Lat-1 channel was pointing at  $118.84^\circ$  (as this channel points  $9^\circ$  to the left of the rover's longitudinal axis). The trajectory was derived by assuming a straight line crossing the different Lat sensor detections, along with the direct light-blocking occurring when all Top sensors have the greatest drop in their corresponding signals. Despite the clear detections carried out by the different RDS sensors and the consistent DD trajectory, this event is unusual at first glance due to the pressure measurements. As discussed in previous works, vortices can be detected by searching for the local drop in pressure expected with the vortex passage (Banfield et al., 2020; Kahanpää & Viúdez-Moreiras, 2021; R. D. Lorenz, 2013; Ordóñez-Etxeberria et al., 2018, 2020). However, and as shown in Figure 4, the pressure measurements did not show a local pressure drop during this event. A possible explanation for this lack of PS detection is that the DD was far from the rover; as we will discuss in the following section, RDS Lat sensors can detect DDs localized at distances as large as 1 km (as long as the DD covers a significant % of the sensor FOV). The Top sensors are more limited in detecting distant DDs due to their more upward-pointing FOV, but it is important to note that, because of the low sun elevation of this event, the blocking of direct light can still occur even if the DD is far from the rover (if this event had not blocked the direct light then the Top sensors would not have displayed any variations in the signals). Thus, all these factors explain the detections made by the RDS Lat and Top sensors and the absence of a local minimum in the PS measurements.



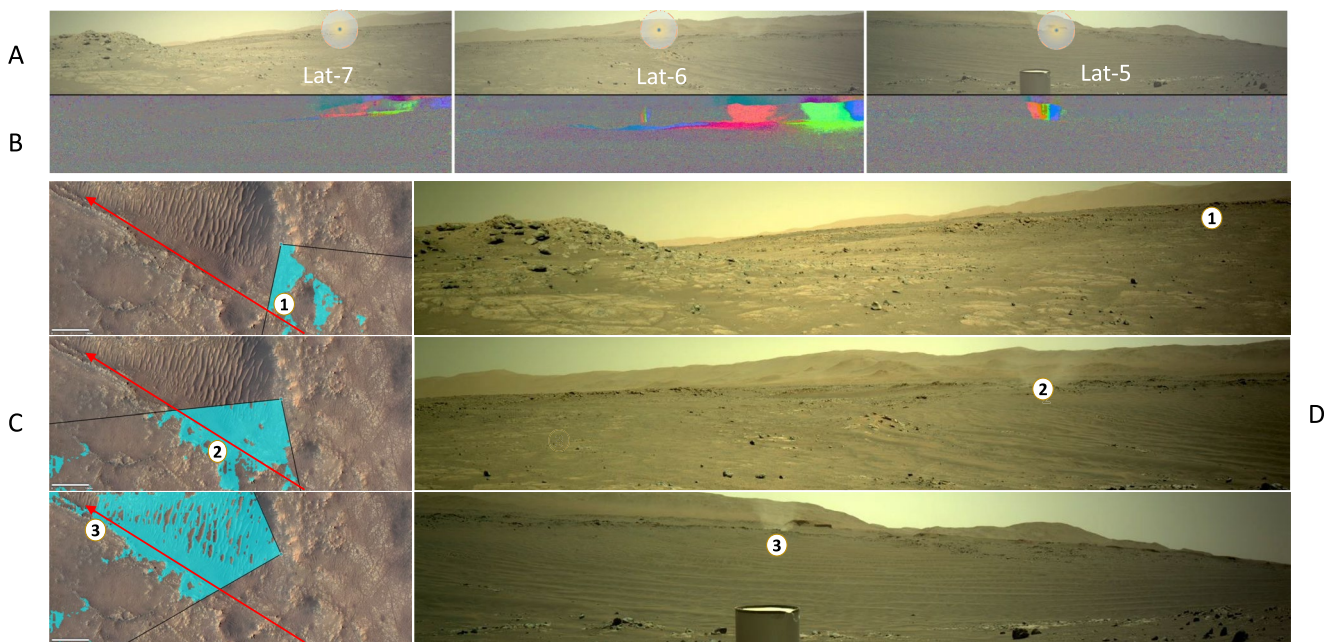
**Figure 4.** Analysis of the first dust devil (DD) detection carried out by RDS on sol 21. The DD produced increases of about 2.5, 8, and 7  $W m^{-2}$  in Lat-8, 7, and 6 sensors, respectively. The decrease observed in Top sensor is due to the block of direct light by the DD.



**Figure 5.** Diagram showing the rover and RDS sensors orientations, along with the possible trajectory of the dust devils shown in Figure 4.

### 2.3. Simultaneous RDS Detections With Navcam

Jezero crater is an active aeolian location (C. E. Newman et al., 2022) that has been intensively analyzed by Perseverance's cameras. In particular, Navcam frequently acquires images of the landscape and horizon (Lemmon et al., 2022; C. E. Newman et al., 2022) with the objective of studying the different DL processes taking place in the area. One of the Navcam observations designed with this objective is the so-called 'dust devil surveys' with five different pointings that survey the complete horizon around the rover with three consecutive images acquired at each pointing. On sol 151 at 13:55 LTST, we were fortunate to follow the progression of a DD past the rover in three of the five image sequences in a Navcam dust devil survey, as well as tracking this with RDS and other MEDA sensors. Figure 6 A (chronological from left to right) shows the three Navcam pointings corresponding with three consecutive sequences where the DD was detected. The three images of each sequence are processed, subtracting the stationary parts of the sequence to emphasize the changing parts (the DD) and then processing the result to highlight these differences. Finally, each processed picture is merged in a



**Figure 6.** On the a panels at top, from left to right, three different sequences (three pictures each, the first of which is shown) for three consecutive RSM clockwise orientations, captured by NavCam consecutively on sol 151 at 13:55 local true solar time, and with looking toward azimuths of 143.98°, 215.99°, and 288.17° in the Mars local frame (North—0°, clockwise). The field of view (FOV) of the RDS Lat sensor relevant to each RSM pointing is shown by the circle. The B panel represent the three pictures of each sequence processed and superimposed to enhance the dust devil (DD) detection: first picture in red, second in green, and third one in blue. The D panels represent the three DD positions (1, 2, and 3) identified on each sequence, selected to derive the trajectory, velocity, and diameter. The C panels at left represent the corresponding DD positions in the topographic map, where the black cone represents the camera FOV and the blue shaded area represents the surface in the line of sight (i.e., visible) to NavCam.

frame (Figure 6 B from left to right), where we can show clearly the passing of the DD over the landscape (first picture in red, then in green, and final in blue). Then, for each sequence we select a picture where the DD is clear visible (Figure 6 D, from up to down) that permits us to characterize its properties. By using the M2020 tools Campaign Analysis Mapping Planning and MMGIS (Calef et al., 2021; Pyrzak et al., 2022) and high-quality topographic maps (Ferguson et al., 2020) represented in Figure 6c, the DD distance and angular position at the locations 1, 2, and 3 were estimated. By following a procedure similar to that described in Greeley et al. (2006), the DD was estimated to be approaching from a heading of  $120.0^\circ \pm 3^\circ$  clockwise from N, with an advection velocity of  $3.70 \pm 0.08$  m/s and  $31.4 \pm 5.2$  m.

This Navcam DD survey was covered by MEDA sensors that were operating at its usual 1-Hz sampling frequency. Figure 7 illustrates the observations made by RDS Lat-6, 7, and 8 sensors, PS, and the wind sensor. The times of the corresponding Navcam images shown in Figure 6 are also represented. Here, we see that RDS Lat-8 is affected by the movement of the RSM during the DD survey, and thus this channel is not considered in the analysis. The Lat-5 sensor is also not in the analysis as it is always affected by Perseverance's High Gain Antenna in its parked position. The first RDS detection was carried out by the Lat-7 sensor at the same time as the first Navcam image. By about 45 s later and between the two first Navcam sequences, Lat-6 displayed an increase in the signal lasting about 16 s. Therefore, the sequence of RDS Lat detections is consistent with Navcam imaging of the DD, as well as with the estimated DD trajectory and velocity. Regarding the RDS Top sensors, none of them with FOVs of  $\pm 15^\circ$  at zenith detected the event, indicating that the DD height is lower than the minimum distance between RDS and the DD divided by  $\tan(15^\circ)$ . Based on the time when the greatest drop in local surface pressure is measured at the rover, and assuming the DD trajectory shown in Figure 6, we estimate a minimum distance of  $\sim 150$  m and thus a DD height smaller than  $\sim 560$  m (assuming a flat surface between the rover and DD). The WS observations indicate changes in wind velocity and direction at the time of closest approach, and the match between the WS and DD inferred wind direction and speed is quite good, despite the large distance ( $\sim 150$  m) between the DD and MEDA sensors. In summary, this example (and other similar cases) contribute to better understand the effect of DDs on RDS signals, as well as to derive information on the DD trajectory from a

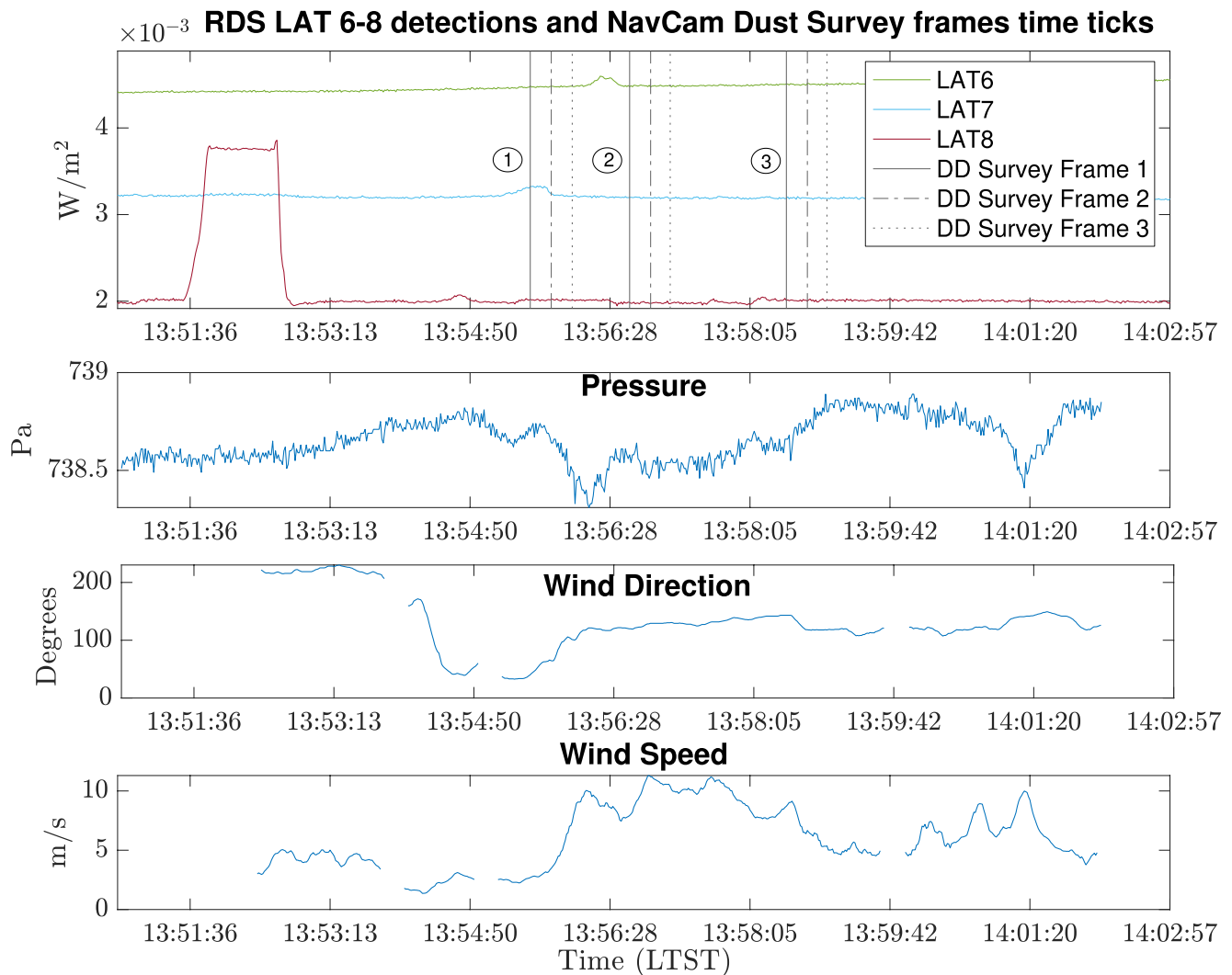


Figure 7. Sol 151 multisensor Detection Event.

sequence of Lat sensor detections. In Section 3.3, we analyze different sequences of Lat detections, for which the DD trajectory was estimated and then compared with the wind sensor observations.

#### 2.4. Radiative Transfer Modeling

In order to study the effect of DDs on RDS signals, we simulated the irradiance measured by the sensors with RT simulations. Because the DD has a finite size and is located at a particular position, we need to evaluate separately its contribution to the total intensity. We performed this calculation in two steps. We first computed with a RT code the source function ( $S_1$ ) for an atmosphere with only airborne dust (without the DD). This is assumed to be the background intensity field. Then, we added the DD as a dust layer (with the same optical properties as the airborne dust) with a height  $h_{DD}$  and column opacity  $\tau_{Total}^{DD}$ , and computed the source function for this other scenario ( $S_2$ ). We then integrated the source function from the surface to the top of the atmosphere using  $S_1$  or  $S_2$  depending on the size of the DD (height and radius), the DD position, and the zenith ( $\theta$ ) and azimuth ( $\phi$ ) angles of observation (a summary of the DD parameters involved in these simulations and in Section 3 is given in Table 1). Note that the use of  $S_2$  in a given height is determined by whether or not there is an intersection between the line of sight from RDS defined by the angles  $\theta$  and  $\phi$  and the DD. Integrating the final intensity field over the FOV of each sensor as detailed in Toledo et al. (2017), we can derive the net effect of the DD on RDS signals. Therefore, for the RT simulations, we need information about the DD radius, height, opacity, optical properties (assumed to



**Table 1**

Summary of the Dust Devil Parameters Involved in the Radiative Transfer Simulations and the Models Described in Section 3

Parameter	Description
$r_{DD}$	Dust devil radius
$h_{DD}$	Dust devil height
$\tau_{DD}$	Dust devil opacity along the direct light direction
$\tau_{Total}^{DD}$	Total dust devil vertical opacity
$n_{DD}$	Number of dust devils crossing the sensor area of detection, expressed in number per units of area and time
$\rho_{DD}$	Dust devil frequency of formation, expressed in number per units of area and time
$l_{RDS}$	Maximum distance at which a given RDS sensor can detect a dust devil
$A_{RDS}$	RDS sensor area of detection, $A_{RDS} = \pi \cdot l_{RDS}^2$
$t_{DD}$	Dust devil life time
$v_{DD}$	Dust devil migration velocity
$\theta_{DD}$	Dust devil migration direction
$\delta$	Angle between $\theta_{DD}$ and the solar azimuth angle
$\tau_{dust}$	Background dust optical depth

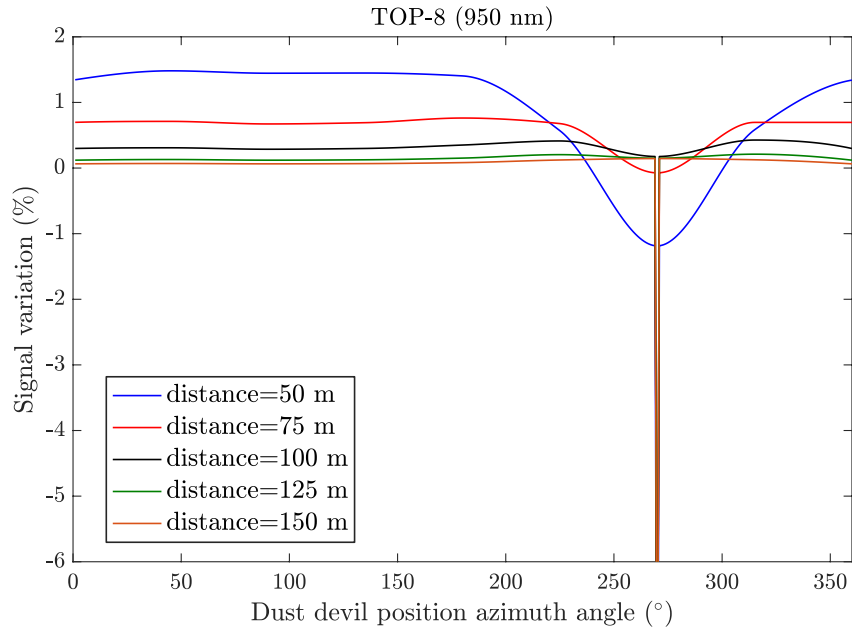
be the same as the airborne dust), and location, along with the properties of the background dust. While the DD height and radius are easy to constrain from observations made by different instruments (e.g., cameras), the range of possible DD opacities ( $\tau_{Total}^{DD}$ ) required for our RT simulations is not easy to estimate. However, for the particular cases in which the DD blocks the direct light but practically does not affect the scattered light received by the Top sensors (like in the case shown in Figure 4), the DD opacity along the direct light direction ( $\tau_{DD}$ ) can be constrained following the procedure described in Appendix A. Once  $\tau_{DD}$  is derived from the observations and assuming that the dust concentration within the DD does not change with radius or height, we can compute  $\tau_{Total}^{DD}$  (needed for the RT simulations) using the following equation:

$$\tau_{Total}^{DD} = \frac{h_{DD}}{2 \cdot r_{DD}} \times \sin(SZA) \times \tau_{DD} \quad (1)$$

where  $r_{DD}$  is the DD radius. This equation comes from the fact that the ratio  $\frac{\tau_{Total}^{DD}}{2 \cdot r_{DD}}$  should be equal to  $\frac{\tau_{DD}}{L}$ , where  $L$  is the length of the direct light path within the DD ( $2 \cdot r_{DD} / \sin(SZA)$ ). Of the total number of detections, only in a few cases, we were able to estimate  $\tau_{DD}$  (e.g., for sol 21 we found a  $\tau_{DD} \sim 0.1$  for  $SZA = 49^\circ$ ), as in most of the direct light-blocking events, the DD covered a significant portion of the sensors FOV (and so they were not far from the rover) and thus affected the scattered light received by the sensors. For the RT simulations of this section, we made use of the  $\tau_{DD}$  derived for the case on sol 21, but in the following sections we will discuss the impact of the uncertainties in this parameter on the results presented in this work.

Figure 8 shows, as example, the impact of a DD, expressed in signal variations compared to the case with only airborne dust ( $\delta S$ ), localized at different azimuth angles and distances on the Top-8 sensor observations. For these simulations the dust optical depth,  $h_{DD}$  and  $r_{DD}$  were fixed to 0.4, 800, and 25 m, respectively. Regarding the sun position, the sun zenith and azimuth angles were set to  $SZA = 10^\circ$  and  $\text{PHI} = 270^\circ$ . These simulations show that depending on the sun and DD azimuth positions and distance RDS-DD, the net effect can be either positive ( $\delta S > 0$ —DD producing an increase in RDS signal) or negative ( $\delta S < 0$ —DD producing a decrease in RDS signal). Note also that the sharp decrease at the DD position azimuth of  $270^\circ$  is due to the blocking of direct light by the DD (DD position azimuth angle =  $\text{PHI}$ ). We see that as the distance becomes smaller, the variation in RDS signal becomes stronger and the range of azimuth angles at which  $\delta S < 0$  is larger. This is due to the fact that the % of the sensor FOV covered by the DD increases as the distance decreases. As we will show in Section 3.5, the DD net effect on RDS signals depends also on the sensor spectral range (as a result of the spectral refractive index of dust particles).

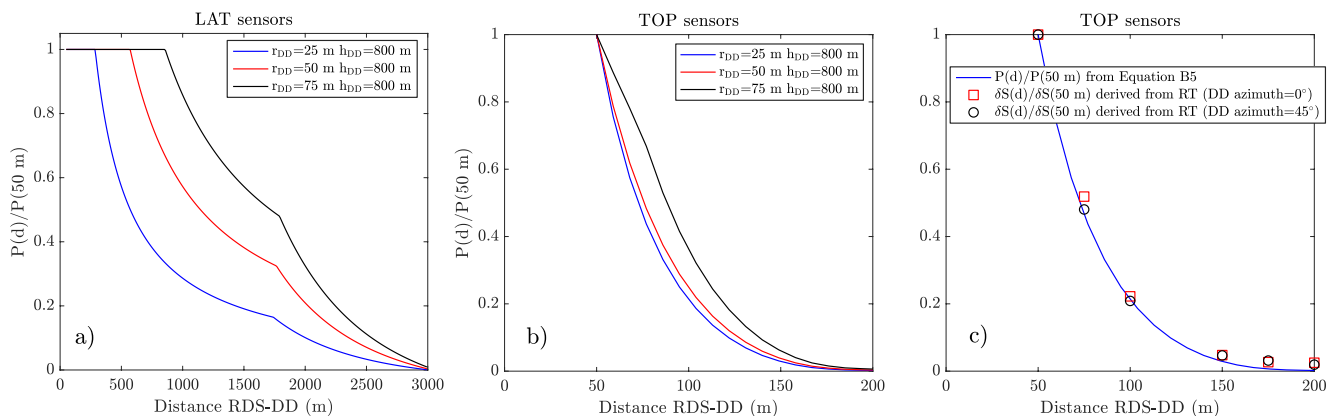
From Figure 8, we also see that for a constant dust-devil-position azimuth angle ( $x$  axis), the variation of  $\delta S$  with distance ( $d$ ) is not linear (similar results were found for the Lat sensors). The main factor controlling this dependence of  $\delta S$  with distance is the % of the sensor FOV ( $P$ ) that is covered by the DD (which also depends on



**Figure 8.** Top-8 signal variation ( $\delta S$ ) simulated for different dust devil (DD) distances and azimuth positions. The DD height and diameter were set to 800 and 50 m, respectively.

the DD dimensions). The analytical equations to compute  $P$  from the distance between RDS and DD and the DD dimensions ( $h_{DD}$  and  $r_{DD}$ ) are provided in Appendix B. Figure 9a shows the variation of  $P$  with distance (normalized by its value when the DD is at a distance of 50 m) for the Lat sensors and for different DD radii. These curves can be divided into three segments according to  $P/P(50\text{ m})$  variation with distance as follows: (a) a first segment in which  $P/P(50\text{ m})$  remains constant and equal to 1 as  $d$  varies and for which the sensor FOV is fully covered by the DD (the extension of this first segment depends on the DD dimensions); (b) a second segment where the sensor FOV is fully covered by the DD height (defined by  $h_{DD}$ ) but not by the DD width (defined by  $r_{DD}$ ); and (c) for the third segment the sensor FOV is not fully covered by either the DD height or width, and it lasts up to the distance where the DD is fully out of the sensor FOV. For the cases shown in Figure 9a, the third segment starts at the same distance as a result of the same DD height.

Similar computations but for the Top sensors (see Appendix B) are illustrated in Figure 9b, where we see that  $P/P(50\text{ m})$  goes to 0 at shorter distances compared with the Lat sensors, meaning that the distance over which DD



**Figure 9.** (a) Variation of  $P$  (normalized by  $P$  at 50 m distance) with distance for Lat sensors computed with Equation B1 for different dust devil (DD) radii. (b) Same as left panel but for Top sensors (computed with Equation B5). (c) Comparison between  $P/P(50\text{ m})$  for Top sensors and the  $\delta S/\delta S(50\text{ m})$  given in Figure 8. As the angular transmission of the sensors varies with the zenith angles, the curve  $P/P(50\text{ m})$  was weighted by the field of view (according to the area covered by the DD).

may be detected is much smaller. We also observe that, as a result of the azimuthal symmetry in the sensor FOV, the  $P$  curves are much simpler compared with the Lat sensors. As we will show in Section 3.5, the DD net effect on RDS signals depends also on the sensor spectral range. In order to estimate the weight of  $P$  on  $\delta S$  (Figure 8), Figure 9c compares the variation of  $\delta S$  with distance (normalized to the value at 50 m) with  $P/P(50\text{ m})$  (weighted by the sensor angular transmission). These results indicate that for constant values of the DD properties (e.g., height or diameter) the main factor controlling the variation of  $\delta S$  with distance is the DD projection over the sensor FOV. As we will discuss in Section 3.3, this result is key for estimating the DD trajectory from a number of Lat detections.

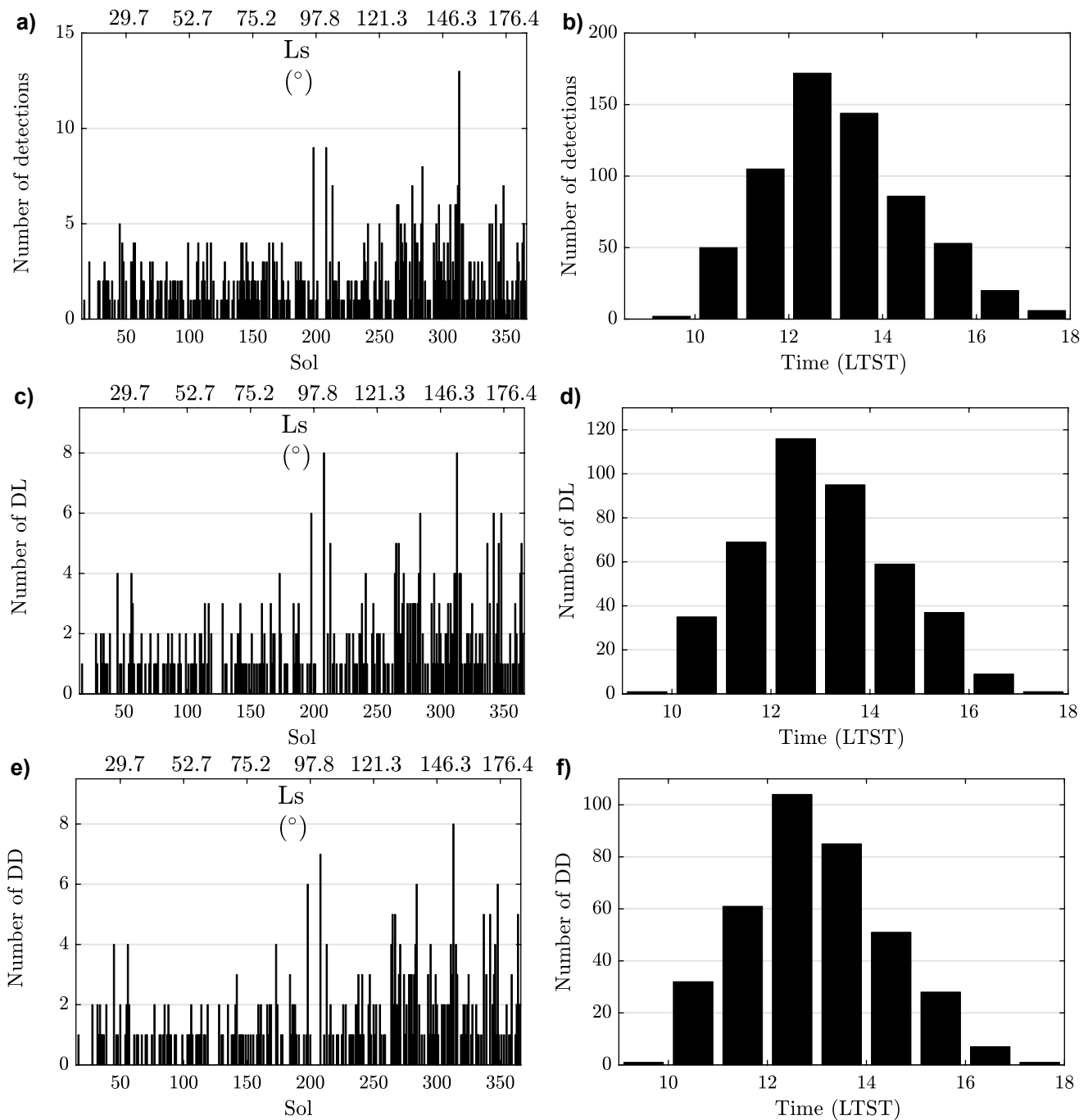
### 2.5. RDS Limit of Detection

The simulations discussed in the previous section are key for evaluating each sensor's limit of detection ( $l_{\text{RDS}}$ ), which is defined as the maximum distance at which a DD can be detected by a particular RDS sensor. This can also be expressed in terms of an area, which for Top channels is given by  $A_{\text{RDS}} = \pi \cdot l_{\text{RDS}}^2$ . From the curves of  $\delta S$  given in Figure 8, we can define the distance at which the DD does not have an impact on the signal. For given values of  $h_{\text{DD}}$ ,  $r_{\text{DD}}$ ,  $\tau_{\text{dust}}$ ,  $\tau_{\text{Total}}^{\text{DD}}$ , and SZA and PH10, we define  $l_{\text{RDS}}$  as the distance at which  $\delta S = 0.1\%$ , a value selected based on the signal noise level and the observed variations in RDS signals caused by DDs. In the case of the Top sensors, whose FOV covers all the azimuth angles (and so different DD azimuth positions,  $x$ -axis of Figure 8), we define  $l_{\text{RDS}}$  as the distance at which  $\delta S \geq 0.1\%$  for at least the 80% of the azimuth angles. For the Top-4 and 8 sensors, for instance, we found  $l_{\text{RDS}} = 67$  and 83 m, respectively, for the same DD properties as in Figure 8 and SZA = 10°. These values change with SZA, and the variation of  $l_{\text{RDS}}$  with the channel comes from the wavelength range of that channel and the spectral optical properties of the dust particles (e.g., M. Wolff et al., 2009). As we will discuss in Section 3.2, the sensor limit of detection (or area) is needed to estimate the DD frequency of occurrence (number of DDs formed per unit area and time) from RDS observations.

## 3. Results

### 3.1. RDS Dust Lifting Detections

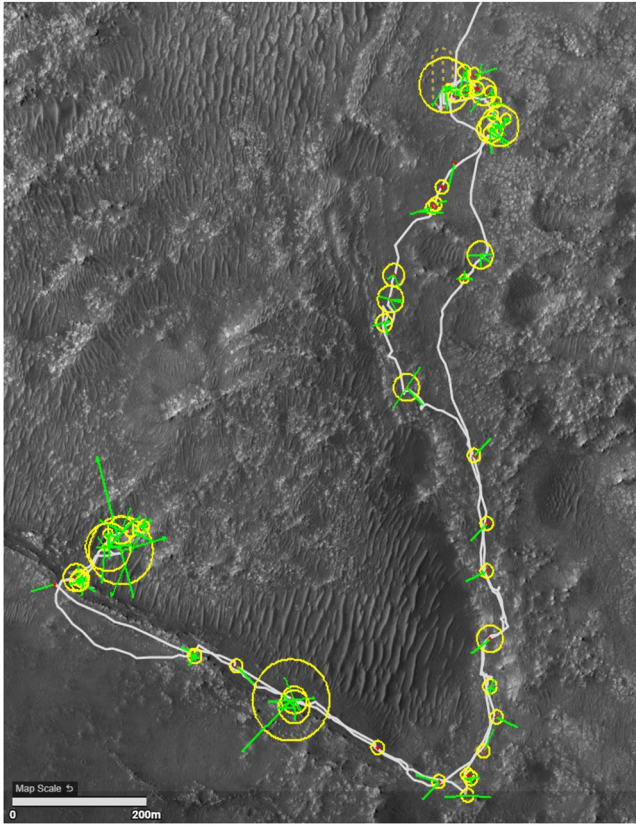
Once the DD signatures in RDS signals were studied and characterized using RT simulations and observations with other instruments, an algorithm was developed to automatically detect the different dust events. This algorithm first fits the RDS observations to a polynomial function to extract from the observations the background signal (the fits are performed over time windows of about 5 min). After subtracting the background signal at each temporal window, the algorithm searches for maxima and minima in the signals with at least 3 consecutive samples below or above the level of noise ( $>3\sigma$ ). Although the original algorithm was capable of detecting signal variations produced by DDs, we also found detection cases that were produced by shadows or movements of different parts of the rover that directly affected the RDS measurements: the High Gain Antenna, for the Lat-5 and Lat-4 channels or the RSM, for the Lat-8 and Lat-7 channels. To filter these events in RDS detections (mostly when the RSM is moving), we developed a 3-D simulator model using Blender (Community, 2018). This includes a model of the rover with its attitude and position of the different moving parts at any time during the mission, along with the relative sun position. Thus, for each detection, we studied the possible interferences with the rover and so discarded the cases that were not produced by DL. Figure 10 a-b shows histograms of all RDS detections per day as a function of sol and the diurnal variation over the first 365 sols ( $L_s = 6^\circ - 182^\circ$ ), employing the RDS algorithm described above. For this statistic, a DD with multiple detections (e.g., a DD crossing 3 different Lat sensors) is counted as one event. Although the diurnal variation of detections is similar to that found for vortices (Hueso et al., 2022), some of them might have not been caused by DDs; for example, a dust cloud that is crossing the Top sensors FOV. For this reason, the detections shown in Figures 10a and 10b were classified into two groups. The first group, called DL, consists of the events that included the following: (a) one or more RDS detections and a local pressure drop caused by a vortex (Hueso et al., 2022) and (b) two or more RDS detections including at least one Lat sensors and for which the PS did not show a drop. The events with simultaneous Lat detections, which are also included in this group, are likely DL produced by wind gusts. Indeed, DL driven by wind gusts can cover a much larger area than most DDs and may be seen in multiple Lat channels at once, whereas DDs are typically only seen by one Lat channel at a time. Therefore, DL includes any kind of DL events, including those produce by DD or by wind gusts. The condition of counting only the cases with at least one Lat detection comes from the fact that these sensors are pointing 20° above the horizon, and so any local DL



**Figure 10.** Histogram of the number of detections (a and b), dust lifting (c and d), and DDs (e and f) performed by RDS. Left panels (a, c, and e) represent the number of cases per sol and right panels (b, d, and f) represent the diurnal variation for the first 356 sols of the mission.

detected by a Top sensor should in principle be registered by at least one of these sensors. The histograms for the DL cases are displayed in Figures 10c and 10d (a total of 426 cases for the full period), which indicate a slightly lower number of cases and a similar diurnal variation (Figure 10d).

The second group of detections, called DD events, represents the cases that are confirmed to be produced by a DD (a total of 374 for the full period); RDS detections including a local pressure drop or sequences of Lat and Top detections that are consistent with the presence of a DD (see examples shown in Figures 4 and 7). To classify an event as a DD without a pressure drop, a minimum of two Lat detections are required, and the



**Figure 11.** Map showing the rover traverse and the locations of the different dust devil detections (normalized by the number of days the rover remained at each location). The yellow and green circles (radii proportional to the number of cases) show the detections carried out by RDS-Top sensors, while the green arrows represents the detections by RDS-Lat sensors (length proportional to the number of detections) and the Lat pointing direction of the first detection. Arrows length were multiplied by a factor 3.6 to facilitate the visualization.

sequence of detections should be consistent with the DD trajectories that will be discussed in Section 3.3. Similar to DL cases, the DD detection peaks at noon (Figures 10e and 10f), with the period between 1200 and 1400 LTST accounting for about the 50% of the total number of cases. Before 10:00 LTST and after 1700 LTST, we found almost no DD activity with just 2 cases out of 370. A table reporting the date and time of each DD detection is provided as supplementary material.

We observe a notable increase in the number of detections in the period between sol 310 and 316, which corresponds to the time when a regional dust storm was actively raising dust in the area containing Jezero crater (Lemmon et al., 2022). Figure 11 displays a map of the rover traverse for the first 365 sols of the Mars 2020 mission, as well as the location of the different DL events detected by RDS-Top (yellow circles) and Lat (green arrows) sensors. The circle and arrow extension is proportional to the number of cases. Here, we see some clusterings in the detections at the lower part of the map as well as at the top right, indicating possible changes in the surface properties, including potentially the surface roughness, thermal inertia or albedo, or grain size distribution. In the next section, the DD frequency of formation will be estimated and the possible changes as a result of the surface or winds will be discussed.

### 3.2. Dust Devil Frequency of Occurrence Derived From the Top Sensors

From the results given in Section 3.1 and the RDS limit of detection (Section 2.5), we can derive the number of DDs detected per unit of area and time for each sensor ( $n_{DD}$ ). However, it is important to note that  $n_{DD}$  does not represent the number of DDs that are formed per unit of area and time (or DD frequency of formation). This results from the fact that not all the DDs detected by RDS are necessarily formed within the sensor area of detection  $A_{RDS}$ . Indeed, in some cases DDs formed away from the instrument can be advected into  $A_{RDS}$ , and thus be detected by RDS despite not forming in that area. The number of such cases depends on the DD speed ( $v_{DD}$ ), trajectory, and lifetime ( $t_{DD}$ ) (R. Lorenz, 2013). In addition to these cases, a DD detection can also occur when the DD is outside  $A_{RDS}$  (they are not close enough to

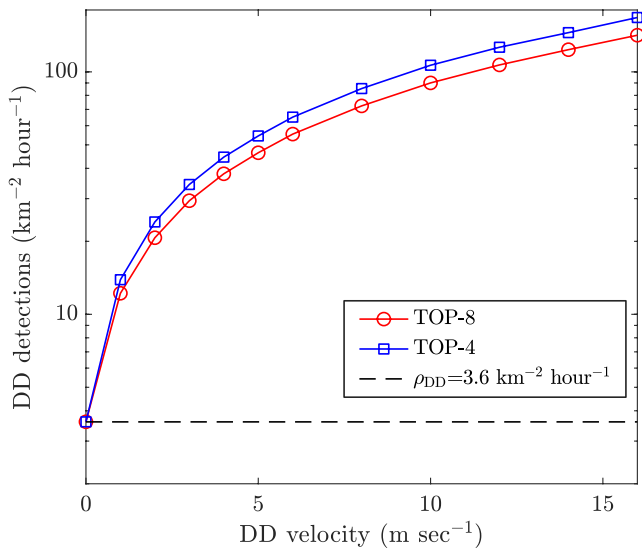
produce a  $\delta S \geq 0.1\%$  in the scattered intensity received by the sensor) but is high enough to block the Sun's direct light (definition of  $A_{RDS}$  in Section 2.5). Note that only the sensors receiving the Sun's direct light can detect these events (e.g., Top sensors). In order to study the impact of all these parameters on RDS detections and the relation between  $n_{DD}$  and DD frequency of formation (referred as  $\rho_{DD}$  thereafter), we performed a number of numerical simulations. In these simulations, we start with an a priori  $\rho_{DD}$  value, and a number of DDs are formed randomly within an area  $A_{max} = \pi \cdot d_{max}^2$ , whose initial coordinates are given by the following equations:

$$x = d_{max} \times \sqrt{r} \times \cos(\Theta) \quad (2)$$

$$y = d_{max} \times \sqrt{r} \times \sin(\Theta) \quad (3)$$

where  $r$  and  $\Theta$  are uniformly distributed variables  $r \in [0,1]$  and  $\Theta \in [0,2\pi]$  and  $d_{max}$  is the maximum distance at which a DD can be formed in the model (referred as MC model thereafter). Note that the square root of  $r$  is used in Equations 2 and 3 in order to have the same number of points (or generated DD) per unit of area. Once a DD is generated, it travels a distance  $d = v_{DD} \cdot t_{DD}$ , assuming a straight line. In the model each DD has associated the DD parameters  $h_{DD}$ ,  $r_{DD}$ ,  $t_{DD}$ ,  $v_{DD}$ , and trajectory. A detection is accounted if the DD crosses the effective area of the sensor or if along its trajectory it blocks the direct light ( $h_{DD} > \text{distance}/\tan(\text{SZA}^\circ)$  and DD azimuth angle = PHIO) for a distance greater than  $l_{RDS}$ . See Appendix C for a complete description of the model.

For the estimation of  $\rho_{DD}$ , we will assume the DD advection velocity and direction can be approximated with the wind sensor observations (Rodriguez-Manfredi et al., 2021). For this reason, only the detections performed



**Figure 12.** Variation of the number of DDs detected per unit of area and time simulated for TOP-4 and TOP-8 sensors, using a dust devil frequency of formation of  $\rho_{DD} = 3.6 \text{ km}^{-2} \text{ hr}^{-1}$ .

by the Top sensors will be used in this analysis as Lat sensors can detect DD found at longer distances for which the WS measurements may not be representative. Figure 12 shows the variation of  $n_{DD}$  with  $v_{DD}$  for the Top-4 and Top-8 sensors, computed with the MC model and using a DD frequency of formation of  $\rho_{DD} = 3.6 \text{ km}^{-2} \text{ hr}^{-1}$ . The DD height, radius, and lifetime were fixed to 800 m, 25 m, and 4 min, respectively. These results show that as the advection velocity increases, the differences between the DD frequency of formation (dashed line) and the number of detections become larger. Note also that the number of detections by the two sensors is different as a result of the different limits of detection (see Section 2.5). Similar results were found when the DD lifetime is increased and, as this parameter is unknown, for the following simulations it is assumed the expression  $t_{DD} = 0.66 \times (2 \times r_{DD})^{0.66}$  derived in R. Lorenz (2013) using data from Earth and Mars. Regarding the direct light-blocking events, the number of cases mainly depends on  $h_{DD}$ , the SZA, and the angle between PHI0 and the DD trajectory ( $\delta$ ). Therefore, the procedure to estimate  $\rho_{DD}$  relies on using these simulations to establish the DD frequency of formation which provides the observed number of detections. If we assume the DD advection velocity and direction can be approximated with the WS observations, then our problem is reduced to two free parameters: the DD height and diameter. As information on these two parameters from RDS observations is limited, we will test different values of them and the variations in  $\rho_{DD}$  will be included in the errors.

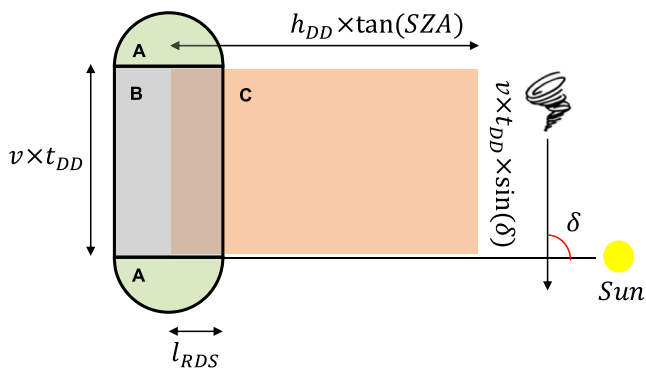
The main problem of using MC to compute  $\rho_{DD}$  is the number of computations required for all the different conditions in which the DD detections occurred (e.g., wind conditions, PHI0, or SZA). However, another way to compute  $\rho_{DD}$  is to estimate the increase in the effective area of the sensor due to winds, the direct light-blocking events, and the DD lifetime. Accounting for these effects, the new effective area (compared with  $\pi \cdot l_{RDS}^2$ ) is given by the following equation:

$$AA = \pi \cdot l_{RDS}^2 + v_{DD} \cdot t_{DD} \cdot C_1 \cdot l_{RDS} + C_2 \cdot v_{DD} \cdot t_{DD} \cdot \text{tg}(SZA) \cdot h_{DD} \cdot \sin(\delta) \quad (4)$$

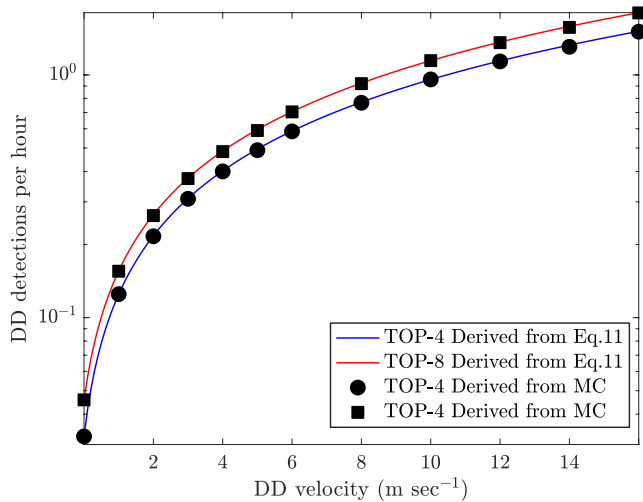
where  $C_1 = 1$  and  $C_2 = 1$  for  $\tan(SZA) \cdot h_{DD} > \frac{l_{RDS}}{\sin(\delta)}$  or  $C_1 = 2$  and  $C_2 = 0$  in the other cases. The three terms on the right side of Equation 4 represent the sensor effective area, the wind advection area (R. Lorenz, 2013), and the area due to the direct light-blocking cases (see Figure 13). Figure 14 shows the variation of DD detections per hour with velocity for Top-4 and Top-5 sensors computed with MC and Equation 4 and for the same conditions as in Figure 12. This comparison shows that both approaches provide similar results, and thus for the estimation of  $\rho_{DD}$ , we will make use of Equation 4. For each RDS Top-4 and Top-8 DD detection, the effective area is computed with Equation 4 using the wind velocity and direction measured by the WS and the corresponding solar angles. In cases for which no wind data are available during the detection time, the average values around that time are used. For the computation of  $l_{RDS}$ , we assumed a dust opacity of 0.4 and different combinations of  $h_{DD}$  and  $r_{DD}$  values, as these parameters are unknown. Therefore, for a given time period  $\Delta t$  the DD frequency of formation is computed as follows:

$$\rho_{DD} = \frac{1}{\Delta t} \sum_1^n \frac{1}{AA_i} \quad (5)$$

where  $n$  is the number of DDs detected by the sensor in  $\Delta t$ , and  $AA_i$  is the effective area of the sensor (computed using Equation 4) for the particular conditions when the detection occurred. The DD frequency of formation was derived for each MEDA block of measurements available (Figure 3) using the detections performed by the Top-4 and Top-8 sensors. Figure 15 shows the daily average (from 10:00 to 17:00 LTST) and diurnal variation of  $\rho_{DD}$



**Figure 13.** Diagram showing the different effective areas for the Top sensors, resulting from (a) DDs formed within  $l_{RDS}$  (in green); (b) DDs formed at distances greater than  $l_{RDS}$  but that are advected into the RDS effective area by the winds (in gray); and (c) the DDs that block the direct light and thus are detected by RDS (in orange). The total effective area is given by the sum of these three areas and removing the overlap between areas B and C.



**Figure 14.** Variation of dust devil (DD) detections per hour with wind velocity for the Top-4 and Top-8 sensors computed using MC model and Equation 4 and using the same DD frequency of formation as in Figure 12.

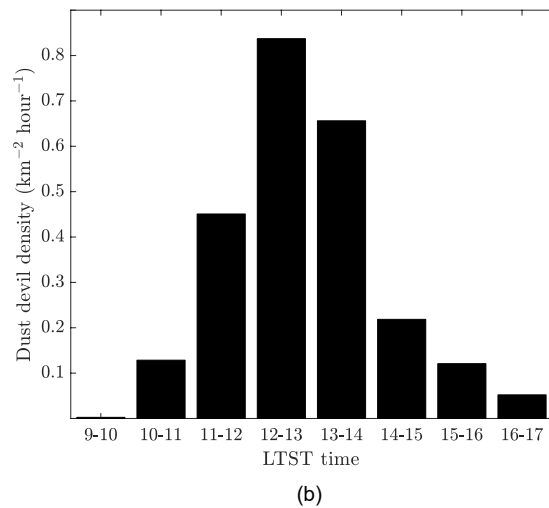
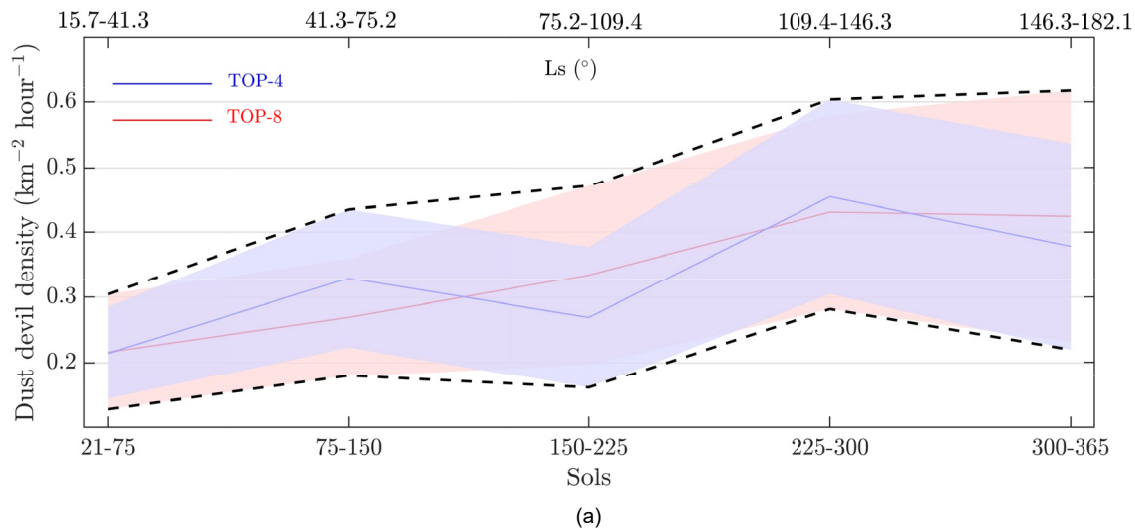
computed for the first 365 sols. The errors were computed based on the uncertainties in  $r_{DD}$ ,  $h_{DD}$ ,  $t_{DD}$ , and  $\tau_{Total}^{DD}$  and their impact on  $\rho_{DD}$  (see Appendix D for more details). Note that although  $l_{RDS}$  depends also on the dust opacity (and in most of the cases it is different to 0.4) because Top sensors detect DDs that are found at not very long distances, the impact of this parameter is negligible compared with the errors caused by the uncertainties in  $r_{DD}$ ,  $h_{DD}$ , and  $t_{DD}$ . In Figure 15, we can see that both sensors provide similar results for the seasonal variations of  $\rho_{DD}$ , namely an increase in the DD activity with sol number or as we move from spring in to summer (where summer begins at  $Ls = 90^\circ$ ). These results are consistent with previous studies (e.g., M. R. Balme et al., 2003; Cantor et al., 2006) that found the peak in DD activity during local summer. C. Newman et al. (2021) used the output from a mesoscale atmospheric model and the Rennó et al. (1998) thermodynamic theory of DD to predict a dust devil activity (DDA) (a measure of the amount of energy that can be harnessed by convective vortices) and predicted a peak in the daily maximum DDA at the landing site location during the mid-to-late summer, which is also in agreement with the results displayed in Figure 15. Note, however, that the rover has visited different regions (Figure 11) with apparent changes in the surface properties, which may also have an impact on the observed DD activity variations along the sols.

Regarding the diurnal variation, we observe the highest DD frequency of formation between 12:00 and 13:00 LTST with values of  $\sim 0.83$  DD per  $km^2$  per hour, which is at least  $\sim 4$  times larger than the frequency of formation found after 14:00 LTST. This period (between 12:00 and 13:00 LTST) follows the peak in solar insolation at local noon and is when the convective heat flux and lower planetary boundary later IR heating are both predicted to peak in Jezero crater (see Figure 16). On the other hand, the lower frequencies are observed at times after 16:00 LTST or before 11:00 LTST, with values below 0.13 DD per  $km^2$  per hour. The time of maximum DD frequency is coincident with that of the vortex activity derived in Jackson (2022), C. E. Newman et al. (2022), and Hueso et al. (2022) from observations made by MEDA PS. However, while Figure 15 shows a notable decrease in  $\rho_{DD}$  after 14:00 LTST, the vortex encounters reported in Jackson (2022) do not indicate a significant decrease after that time. This suggests that the decrease in  $\rho_{DD}$  observed after 14:00 LTST is not due to a decline in the vortex activity but is rather due to the number of vortices capable of lifting dust. We also studied the diurnal variation of  $\rho_{DD}$  but for periods of 60 sols (instead of for the 365 sols), and similar results were found; a maximum between 12:00 and 13:00 LTST, and no more peaks after this period or before noon. From these results, we derive a DD frequency of formation at Jezero between 1.3 and 3.4 DD per  $km^2$  and sol. These results are in agreement with the DD frequency of between 2.0 and 3.0 DD per  $km^2$  and sol derived in Hueso et al. (2022) from an independent estimation.

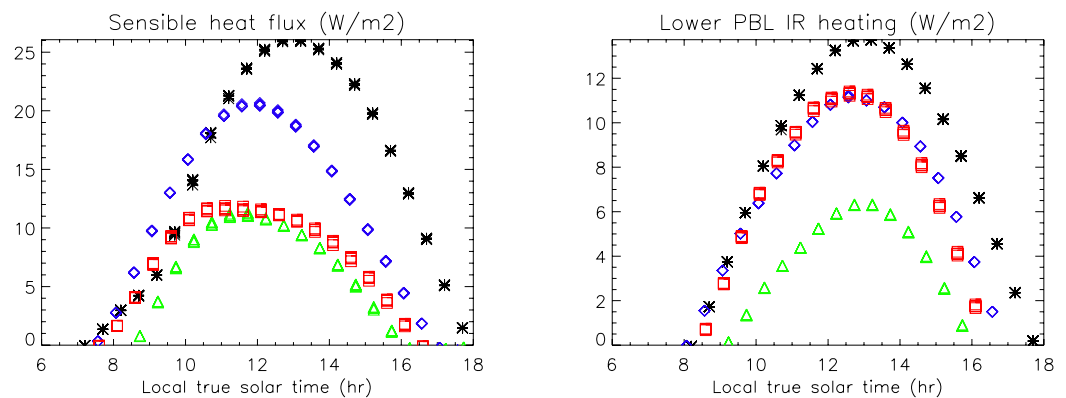
### 3.3. Dust Devil Trajectory Analysis

Dust Devil size and trajectory characterization has previously been studied using in situ observations. Typically, those studies have been performed using cameras (e.g., Ferri et al., 2003; Greeley et al., 2006; Metzger et al., 2000; Moores et al., 2015), pressure sensors (e.g., Kahanpää et al., 2016), or a combination of meteorological sensors (e.g., Kahanpää & Viúdez-Moreiras, 2021; R. D. Lorenz, 2016). In this section, we investigate the possibility for estimating information on the DD properties (e.g., diameter and trajectory) when a sequence of RDS detections occur for the same event. To this end, a model that computes the expected signal variations when a DD crosses the FOV of different RDS sensors was developed. Because of the large simulation time that would be required, this model does not make use of RT simulations. As demonstrated in Section 2.4, most of the RDS signal variations produced by a DD comes from the changes in the DD projection over the sensor FOV (see Equations B1–B5 and Figure 9). Therefore, for a given DD velocity, trajectory, and diameter we can make use of the results discussed in Section 2.4 to compute the expected signal variations.

For each detection performed by any of the Lat sensors, the model first searches for the times when the detection starts ( $t_{(1)}$ ), finishes ( $t_{(2)}$ ), and reaches the signal maximum ( $t_{(3)}$ ). These times are assumed to be the moments when (a) the DD enters the sensor FOV; (b) the DD leaves the sensor FOV; and (c) the DD is at the center of the sensor FOV (maximum of transmission). With respect to the Top sensor detections, if any, we only study the cases when

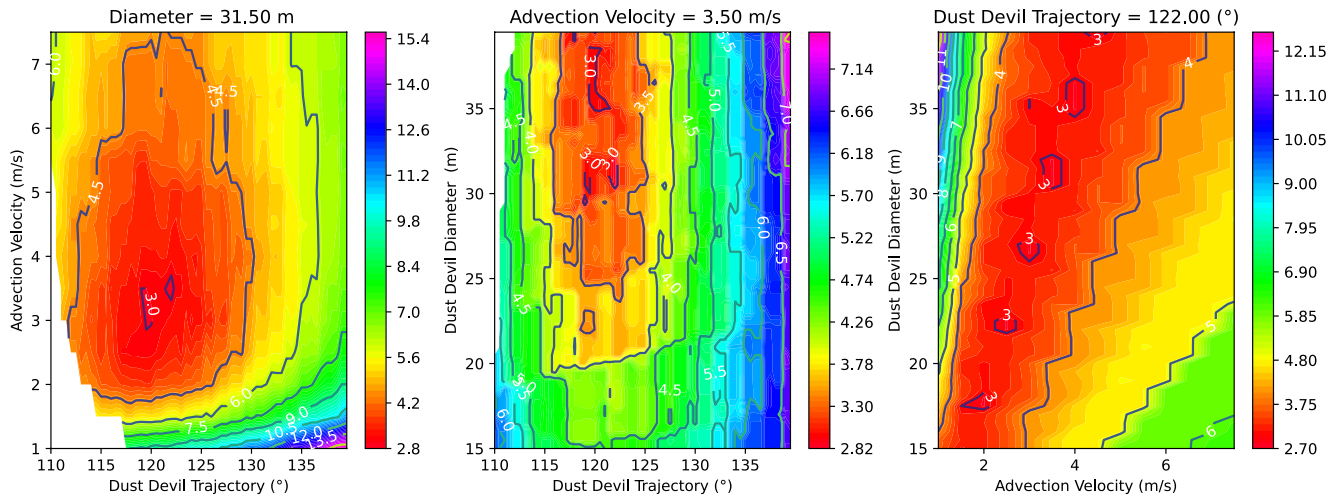


**Figure 15.** (a) Seasonal variation of the dust devils (DDs) frequency of formation ( $\rho_{DD}$ ) calculated by applying Equations 4 and 5 to the DD detection cases shown in Figure 10 (using only the Top-4 and Top-8 detections). Errors, which are represented by the shaded areas, were computed using the procedure described in Appendix D. (b) Diurnal variation of the DD frequency of formation for the whole 365-sols period.



**Figure 16.** Diurnal variation of sensible heat flux and lower planetary boundary later IR heating predicted for the Mars 2020 (black), InSight (blue), Spirit (green), and Opportunity (red) landing sites and  $L_s = 90^\circ$ . These simulations were performed using the model described in C. E. Newman et al. (2019) and C. Newman et al. (2021).





**Figure 17.** Contours of  $\chi^2$  in the  $\theta_{DD}$ - $v_{DD}$  space (left panel),  $\theta_{DD}$ - $r_{DD}$  space (central panel), and  $v_{DD}$ - $r_{DD}$  space (right panel) for the solution  $r_{DD} = 15.75$  m,  $v_{DD} = 3.5$  m/s, and  $\theta_{DD} = 122^\circ$ . The white area of left panel indicates the combinations of  $\theta_{DD}$ - $v_{DD}$  that are not valid for  $r_{DD} = 15.75$  m.

a direct light-blocking is registered (similar to that shown in Figure 4). In the direct light-blocking cases, the DD azimuth angle is the same as PH10 at the time of the Top sensor detection. Note that all these times depend on the DD diameter, advection velocity, and trajectory. Therefore, all these DD properties are considered as free parameters in the model. For the intersection times between the DD and the sensor FOV, we assume that the DD is a perfect cylinder with a constant diameter.

The trajectory is assumed to be a straight line, whose parameters are the angle clockwise with respect to the north and the distance from the DD to the rover. Although for some cases a straight line may not represent the real DD trajectory, a more complex curve would result in an increase in the number of model free parameters and thus a high degree of degeneracy in our best fit solutions. In order to better constrain the DD properties, the model also uses the PS detections; the time of the pressure local minimum occurs at the moment of closest approach between the rover and the DD. Once the sequence of time detections is provided for a given event, then the model searches for the DD trajectory, velocity, and diameter that minimizes the  $\chi^2$  function defined as follows:

$$\chi^2(r_{DD}, v_{DD}, \text{distance}) = \left\{ \frac{\sum_1^n (t_i^* - t_i)^2}{n_{\text{Total}}} \right\}_1 + \left\{ \frac{(t_{n+1}^* - t_{n+1})^2}{n_{\text{Total}}} \right\}_2 + \left\{ \frac{(t_{n+2}^* - t_{n+2})^2}{n_{\text{Total}}} \right\}_3 + F \quad (6)$$

where  $t_i$  and  $t_i^*$  represent the measured and simulated times of (a) the  $n$  Lat sensor detections (first term on the right-hand side); (b) the direct light-blocking produced by the DD (second term on the right-hand side), if any; and (c) the closest approach between the DD and the rover (third term on the right-hand side) established from the local pressure drop. Note that for each Lat detection three different times are fitted with the model ( $t_{(1)}$ ,  $t_{(2)}$ , and  $t_{(3)}$ ). The last term on the right-hand side of Equation 6 (F) is a penalty function that takes a value of 9,000 s for the solutions which are not compatible with the observations (i.e., a simulated detection which is not observed by RDS), and  $n_{\text{Total}}$  is the total of times to fit. If the event does not include a direct light-blocking, then  $t_{n+1} = 0$ .

The DD detected on sol 151 shown in Figure 7 was analyzed with this model, accounting for the two Lat detections and the local pressure drop. A number of combinations of  $v_{DD}$ ,  $r_{DD}$ , and DD direction ( $\theta_{DD}$ ) were used to compute the times  $t_i^*$  of Equation 6 and then the values of  $\chi^2$  were studied. We found that while  $\theta_{DD}$  is well constrained in this analysis, the parameters  $v_{DD}$  and  $r_{DD}$  are correlated, and then there is a degeneracy in the solution space. Figure 17 displays, as example, contour plots of Equation 6 in the  $\theta_{DD}$ - $v_{DD}$ ,  $\theta_{DD}$ - $r_{DD}$ , and  $v_{DD}$ - $r_{DD}$  spaces for the case of sol 151 and for  $r_{DD} = 15.75$  m (left panel),  $v_{DD} = 3.5$  m/s (central panel), and  $\theta_{DD} = 122^\circ$  (right panel), which is one of the combinations that minimizes  $\chi^2$ . Here, we see that optimum

**Table 2**

Comparison Between Dust Devils Migration Direction and Surface Wind Direction for Different Cases

Sol	SCLK	LTST	Avg. background velocity (m/s)	Avg. background direction	DD trajectory	DD diameter (m)	DD trajectory deviation respect to wind direction (min, max)	DD diameter from background velocity (m)
39	670412297	14:43:05	6.6 ± 2.0	97.8° ± 10.0°	104° ± 1°	$d_{DD} = 1.24 \cdot v_{DD} + 1.22 R^2 = 0.81$	[0°–17.2°]	9.4 ± 2.5
127	678211562	11:42:09	4.8 ± 1.8	89.4° ± 13.0°	92° ± 1°	$d_{DD} = 2.00 \cdot v_{DD} + 5.00 R^2 = 0.49$	[0°–16.6°]	14.6 ± 3.6
151	680350036	13:55:20	6.4 ± 2.0	123.0° ± 12.6°	122° ± 1°	$d_{DD} = 8.88 \cdot v_{DD} + 0.06 R^2 = 0.99$	[0°–14.6°]	56.9 ± 17.8
158	680968291	13:05:17	7.2 ± 0.9	117.6° ± 7.6°	120° ± 2°	$d_{DD} = 4.52 \cdot v_{DD} R^2 = 0.99$	[0°–12.0°]	32.5 ± 4.1
178	682741651	12:34:10	5.4 ± 1.7	153.5° ± 16.2°	163° ± 1°	$d_{DD} = 1.50 \cdot v_{DD} + 0.50 R^2 = 0.75$	[0°–26.7°]	8.6 ± 2.6
208	685406867	13:10:31	4.7 ± 2.1	117.7° ± 47.8°	75° ± 1°	$d_{DD} = 7.28 \cdot v_{DD} + 0.10 R^2 = 0.99$	[0°–91.5°]	34.3 ± 15.3
241	688336509	13:16:15	5.4 ± 2.3	72.7° ± 43.1°	100° ± 1°	$d_{DD} = 9.10 \cdot v_{DD} + 0.86 R^2 = 0.87$	[0°–71.4°]	50.0 ± 20.9
271	690993849	11:44:59	3.4 ± 1.5	94.9° ± 68.9°	90° ± 2°	$d_{DD} = 0.34 \cdot v_{DD} + 0.10 R^2 = 0.95$	[0°–75.8°]	1.3 ± 0.5
283	692059639	11:54:54	4.3 ± 2.5	132.2° ± 60.0°	115° ± 3°	$d_{DD} = 5.58 \cdot v_{DD} + 5.52 R^2 = 0.85$	[0°–80.2°]	29.4 ± 14.0
312	694630823	11:06:23	2.7 ± 1.9	224.8° ± 67.5°	215° ± 2°	$d_{DD} = 5.90 \cdot v_{DD} + 1.26 R^2 = 0.90$	[0°–79.3°]	17.2 ± 11.2

Note. The relationship between the DD diameter and advection velocity is also given, based on the solution space of Equation 6, and from the wind velocity measurements, an estimation of the DD diameter is given. In the latter calculation, it is assumed that the DD is advected at the wind velocity.

solutions of  $\theta_{DD}$  are found for a narrow range of angles and also that  $r_{DD}$  and  $v_{DD}$  are linearly correlated (right panel). The straight line given by  $r_{DD} = 4.44 \cdot v_{DD} + 0.027$  provides the  $r_{DD}$ - $v_{DD}$  combinations that minimizes  $\chi^2$  for  $\theta_{DD} = 122^\circ$ .

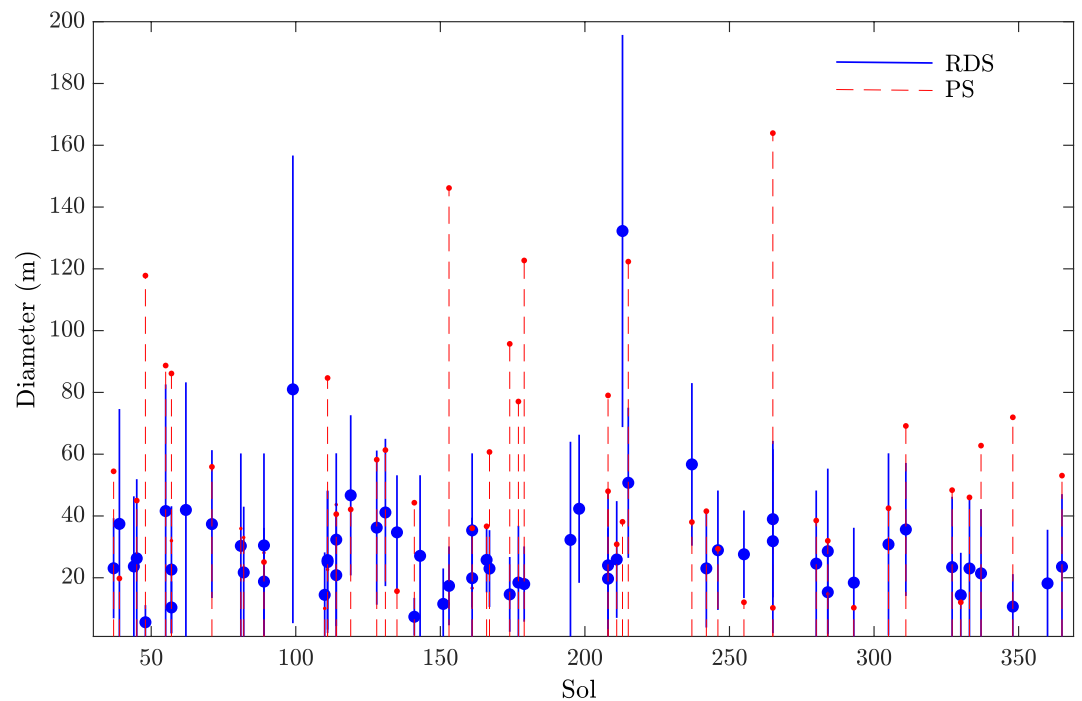
This solution is in agreement with the analysis of Figure 6 for which we derived a DD trajectory of  $120^\circ \pm 3^\circ$  and  $v_{DD}$ - $r_{DD}$  values of  $3.7 \pm 0.08 \text{ m s}^{-1}$  and  $15.7 \pm 2.6 \text{ m}$  that lie within the derived straight line. By comparing these results with Figure 7, we see that the DD trajectory is similar to the wind direction and velocity measurements seconds after the maximum approach. Therefore, this analysis shows that from a sequence of Lat detections, we can estimate the trajectory of the DD and the relationship between the DD radius and advection velocity and then compare them with the wind measurements. A similar analysis was performed for a number of different DD detection cases, whose results are summarized in Table 2. These results show that in general the DD migration direction and surface wind direction are in agreement (to  $\sim \pm 10^\circ$ ). In all the cases the DD diameter and advection velocities were linearly correlated, and so they could not be estimated from RDS observations alone. Because of the correlation between these parameters, only a straight-line relationship was given for each case (along with the coefficient of determination obtained).

### 3.4. Dust Devil Diameter, Lifetime, and Height Characterization

Quantifying the DD contribution to the Martian dust budget requires that we estimate not only DD frequency of occurrence but also the dimensions and lifetime of each event. However, information on DD sizes from RDS observations is very limited. Only in a few cases, for which wind measurements are available, can the DD diameter and height be constrained. As discussed in Section 3.2, a number of the detections shown in Figure 10 correspond to scenarios for which the sun direct light was blocked by the DD. In these particular cases, the detection is characterized by a steep drop in the signal (see next section) whose duration depends on the DD diameter, the advection velocity, and the angle between the DD trajectory and the solar azimuth (Kahanpää & Viúdez-Moreiras, 2021). If we approximate the DD advection speed and direction based on simultaneous wind sensor data, then we have the following equation:

$$r_{DD} = \frac{v_{DD} \cdot \Delta t^* \cdot \sin(\delta)}{2} \quad (7)$$

where, as in Equation 4,  $\delta$  represents the angle between the DD trajectory and PH10. Of the statistics illustrated in Figure 10, only a few % of the cases presented direct light-blocking, whose analysis provided the DD diameters given in Figure 18 (blue lines) and Table 3. The 5 min average of the wind velocity and direction was used in Equation 7, and the standard deviations of these parameters were employed to compute the errors. In most of



**Figure 18.** Dust devil diameters estimated using Equation 7 for the direct light-blocking cases. For comparison purposes, the figure also shows the diameters using the pressure sensor observations.

**Table 3**  
*Dust Devil Diameters Estimated Using Equation 7 for the Direct Light-Blocking Cases*

Sol	SCLK	DD diameter (m)	Sol	SCLK	DD diameter (m)	Sol	SCLK	DD diameter (m)
37	670232977	23.1 ± 16.2	128	678302747	36.2 ± 25.0	237	687975280	56.7 ± 26.3
39	670412344	37.4 ± 37.2	131	678567469	41.1 ± 23.8	242	688426062	23.0 ± 19.1
44	670846889	23.7 ± 22.7	135	678923082	34.7 ± 18.5	246	688777425	28.9 ± 19.3
45	670933103	26.3 ± 25.6	141	679453063	7.4 ± 6.1	255	689581269	27.6 ± 14.2
48	671207441	5.6 ± 5.5	143	679631617	27.1 ± 26.1	265	690461977	39.0 ± 25.3
55	671824637	41.6 ± 41.0	151	680342956	11.5 ± 11.5	265	690467979	31.8 ± 29.8
57	671995983	22.6 ± 20.5	153	680525575	17.4 ± 12.8	280	691799191	24.6 ± 23.7
57	672002166	10.4 ± 8.5	161	681235202	35.4 ± 24.9	284	692143596	15.3 ± 14.5
62	672444830	42.0 ± 41.3	161	681237808	19.9 ± 19.6	284	692153092	28.6 ± 26.7
71	673245882	37.4 ± 23.9	166	681678408	25.8 ± 10.5	293	692953281	18.4 ± 17.8
81	674133320	30.3 ± 29.9	167	681768311	23.0 ± 12.4	305	694018848	30.8 ± 29.5
82	674218888	21.7 ± 21.3	174	682380468	14.6 ± 12.1	311	694546430	35.6 ± 21.5
89	674843562	30.5 ± 29.8	177	682649434	18.4 ± 18.4	327	695969394	23.4 ± 22.8
89	674850856	18.8 ± 17.4	179	682824016	18.0 ± 12.2	330	696228563	14.4 ± 13.7
99	675732309	81.0 ± 75.7	195	684247546	32.3 ± 31.8	333	696499462	23.0 ± 22.4
110	676713166	14.5 ± 13.7	198	684517058	42.3 ± 24.0	337	696861425	21.4 ± 20.8
111	676798569	25.7 ± 22.5	208	685406019	24.0 ± 23.5	348	697826179	10.7 ± 10.5
111	676799961	25.1 ± 23.0	208	685406923	19.7 ± 16.3	360	698891309	18.2 ± 17.4
114	677055259	20.9 ± 20.5	211	685668823	25.9 ± 18.9	365	699331347	23.6 ± 23.5
114	677067864	32.3 ± 28.0	213	685853656	132.2 ± 63.5	–	–	–
119	677501518	46.7 ± 25.9	215	686017624	50.7 ± 24.3	–	–	–

these cases, DD diameters were smaller than 60 m and with no particular seasonal trend (information is limited by the errors), and on average we found  $d_{DD} = 29$  m (or a median diameter of 25 m). The maximum diameter for these cases is found for sol 213 with  $d_{DD} = 132 \pm 63.4$  m, while the minimum diameter was reported on sol 48 with  $d_{DD} = 5.6 \pm 5.5$  m. These numbers are also in agreement with those given in Hueso et al. (2022) which are based on Monte-Carlo modeling pressure and wind data of vortices including the large event on sol 213.

For comparison purposes, the DD diameter was also estimated from MEDA PS measurements and the vortex model described in R. D. Lorenz (2016) (red dashed lines in Figure 18). To simplify the calculations only the pressure observations were used to constrain  $d_{DD}$ , and for this reason only an upper limit of  $d_{DD}$  was estimated (red dashed lines in Figure 18). Although in some cases the DD diameter is poorly constrained, we see that in general both diameter estimations are in agreement (only for two cases out of 60, do the two approaches provide different  $d_{DD}$ ). If we assume the DD lifetime can be approximated as  $t_{DD} = 0.66 \times (2 \times r_{DD})^{0.66}$  (R. Lorenz, 2013), then from the results in Figure 18 we find an average  $t_{DD}$  of  $\sim 6$  min.

Information on the DD height can also be estimated from the time duration of the Top sensor detections. Given a DD at a given distance  $d$  from RDS and excluding the direct light-blocking cases, a Top sensor detection occurs only if the DD height is greater than  $d/\tan(15^\circ)$  (otherwise there is no intersection between the sensor FOV and the DD). If we assume the DD crosses the sensor FOV through the center (or at a zenith angle of the sensor FOV of  $0^\circ$ ), then the DD height is given by the following equation:

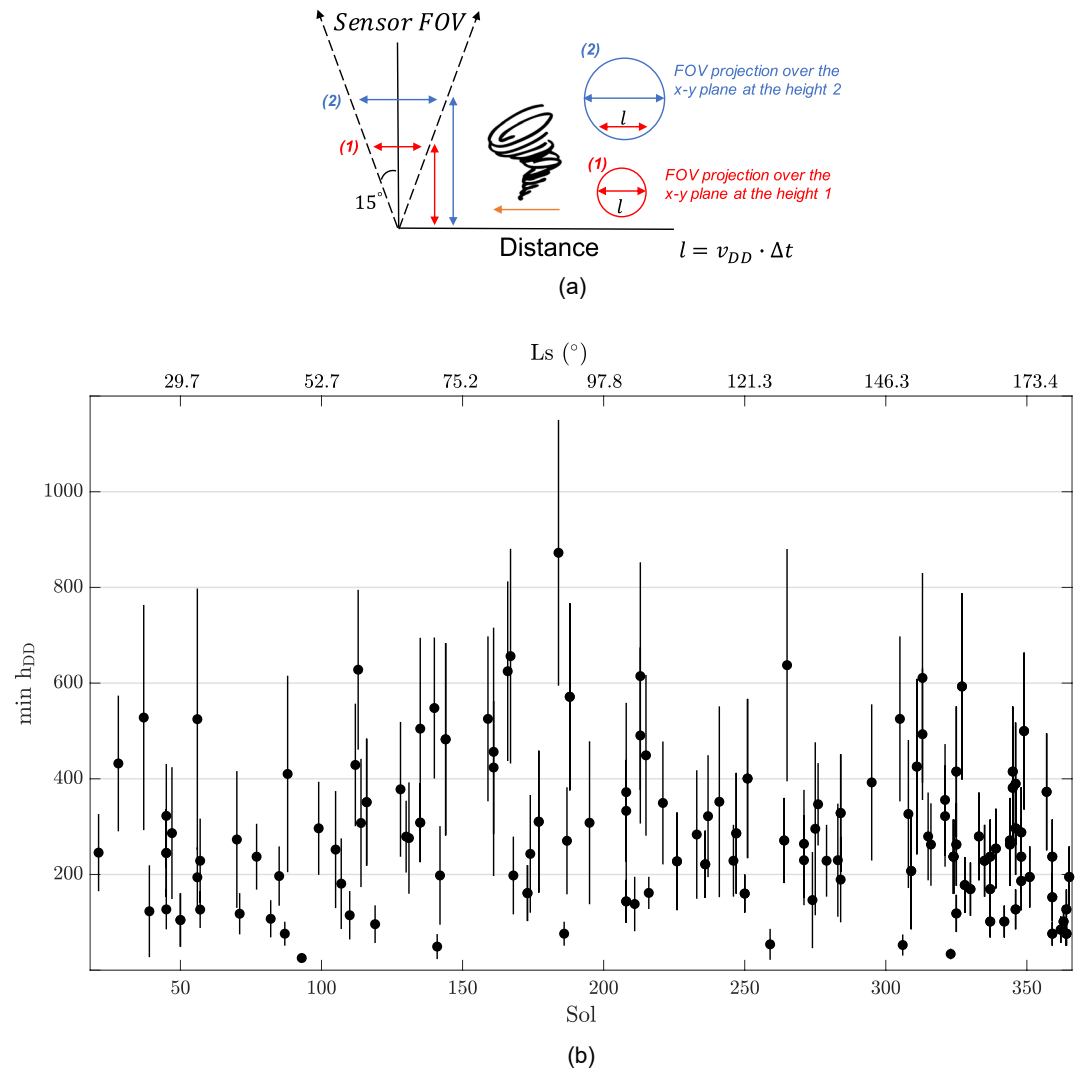
$$h_{DD} = \frac{v_{DD} \cdot \Delta t}{2 \cdot \tan(15^\circ)} \quad (8)$$

where  $\Delta t$  is the detection time duration (see diagram in the right panel of Figure B3 and in the upper panel of Figure 19). In most of the cases, however, the DD does not cross the sensor FOV (whose projection over a  $x$ - $y$  plane is a circle as shown in the upper panel of Figure 19) through the center, and thus Equation 8 does not represent the real height of the DD. Taking into account the fact that the longest straight line inside a circle is the one that intercepts the center, we find that for a given  $v_{DD} \cdot \Delta t$  value, Equation 8 represents the minimum DD height. Indeed, if the DD does not cross the sensor FOV through the center, then the intersection between the DD and the FOV should occur at a greater height (see top panel of Figure 19). Note that for this analysis we are only considering the Top sensors with a FOV of  $\pm 15^\circ$  at zenith, and so the TOP-7 sensor is excluded. The Top panel of Figure 19 shows the minimum heights estimated for Top sensors observations for the first 365 sols. Overall, the mean minimum height is found to be  $\sim 231$  m and for about 16% of the cases  $\min(h_{DD}) > 400$  m. This analysis also indicates higher  $\min(h_{DD})$  during the period between sol 125 and sol 225, a result that may be related to the variation of the boundary layer height, which may in turn be related to the circulation in the specific Ls range or the properties of the surface over which the rover traveled in those sols.

### 3.5. Dust Devil Effect on Irradiance Observations

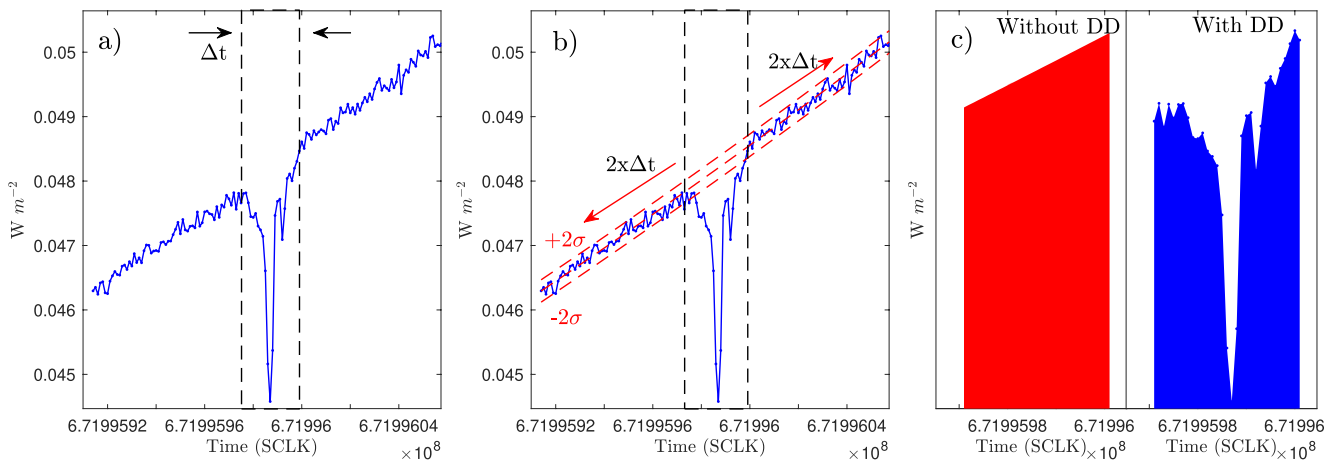
The effect of DDs on the irradiance levels measured by RDS was studied for the DD detections shown in the lower panel of Figure 10. We observed that, depending on the event and the sensor wavelength, the net effect of DD on the irradiance measurements can be positive or negative. To quantify the variations in the irradiance produced by the DD, we selected for each event a time window  $\Delta t$  centered at the minimum or maximum of the signal change (see Figure 20a). The extension of  $\Delta t$  is established such that 80% of the observations in that time window are outside the  $3\sigma$  level (3 times the signal standard deviation) outside the minimum or maximum. To estimate the irradiance values across the period covered by  $\Delta t$  that would have been experienced in the absence of the DD, we fitted the RDS signal to a polynomial function but using only the observations outside  $\Delta t$  (Figure 20b). This fitted signal represents the irradiance for the case without the DD, and thus by integrating both the fitted signal and the observed signal over  $\Delta t$  (giving the integrated irradiance over time, IIOT, for both the cases without and with a DD), we can estimate the net radiative impact of the DD at the rover location. Figure 20c compares the areas obtained for the cases with (in blue) and without (in red) a DD, and for which the DD net effect was found to be  $-22 \text{ J m}^{-2}$  or  $-2\%$  of the integrated irradiance (calculated with respect to the case without DD).

A similar analysis was performed for all the detection cases involving the Top-7 sensor (190–1,200 nm), whose results are illustrated in Figure 21. Here, we see that in UV wavelengths all DD events resulted in a decrease in IIOT (with respect to the case without a DD) with average drops of  $-0.438\%$ ,  $-0.622\%$ , and  $-0.620\%$  for the Top-1, Top-2, and Top-3 sensors, respectively. On the contrary, the events registered by Top-8 displayed both



**Figure 19.** (a) Diagram showing two intersection heights between the Top sensor field of view (FOV) and a dust devil (DD). If the DD crosses the Top sensor FOV through the center, then the DD height is given by Equation 8. If the DD does not cross the Top sensor FOV through the center, then the DD height should be greater than that given by Equation 8. Indeed, if the DD height was lower than the height from Equation 8, then the length  $v_{DD} \cdot \Delta t$  would be greater than the diameter of the FOV projection over the x-y plane at the DD height, which is not possible. (b) Minimum DD heights estimated using Equation 8. As in the previous analyses the DD advection velocity and trajectory was approximated using the wind sensors measurements.

positive and negative variations in the integrated irradiance, depending on the DD and sun angular positions; from the simulations discussed in Section 2.4, we inferred that DDs affecting the forward scattering had a negative impact on the observations, while those affecting the backward scattering resulted in increases in the irradiance. On average, we find a reduction in IIOT value (with respect to the case without a DD) of  $-0.268\%$  for Top-8, the absolute magnitude of which is smaller than that at UV ranges due to the different dust scattering properties. The main reason why in the UV the DD only produced decreases in the irradiance observations comes from the fact that dust particles are very absorbing at UV wavelengths (M. Wolff et al., 2009; M. J. Wolff et al., 2010), and so most of the light received by these sensors comes from the direct light or the light scattered at small scattering angles. Therefore, the detection carried out by UV sensors corresponds to direct light-blocking events or DD mostly affecting the forward scattering. On the contrary, at visible or near IR wavelengths, dust particles are much less absorbing (or much brighter), and thus the contribution of the scattered light at different angles to the total irradiance measured by these sensors is much greater compared with the UV sensors. Therefore, the detections



**Figure 20.** (a) RDS signal drop of about 24 s produced by the presence of a dust devil (DD). The sharp decrease can be produced by the blocking of the direct or scattered light. (b) Selection of RDS observations affected by the DD through the standard deviation ( $\sigma$ ). (c) Comparison between areas ( $W$ ) for the cases with and without the DD.

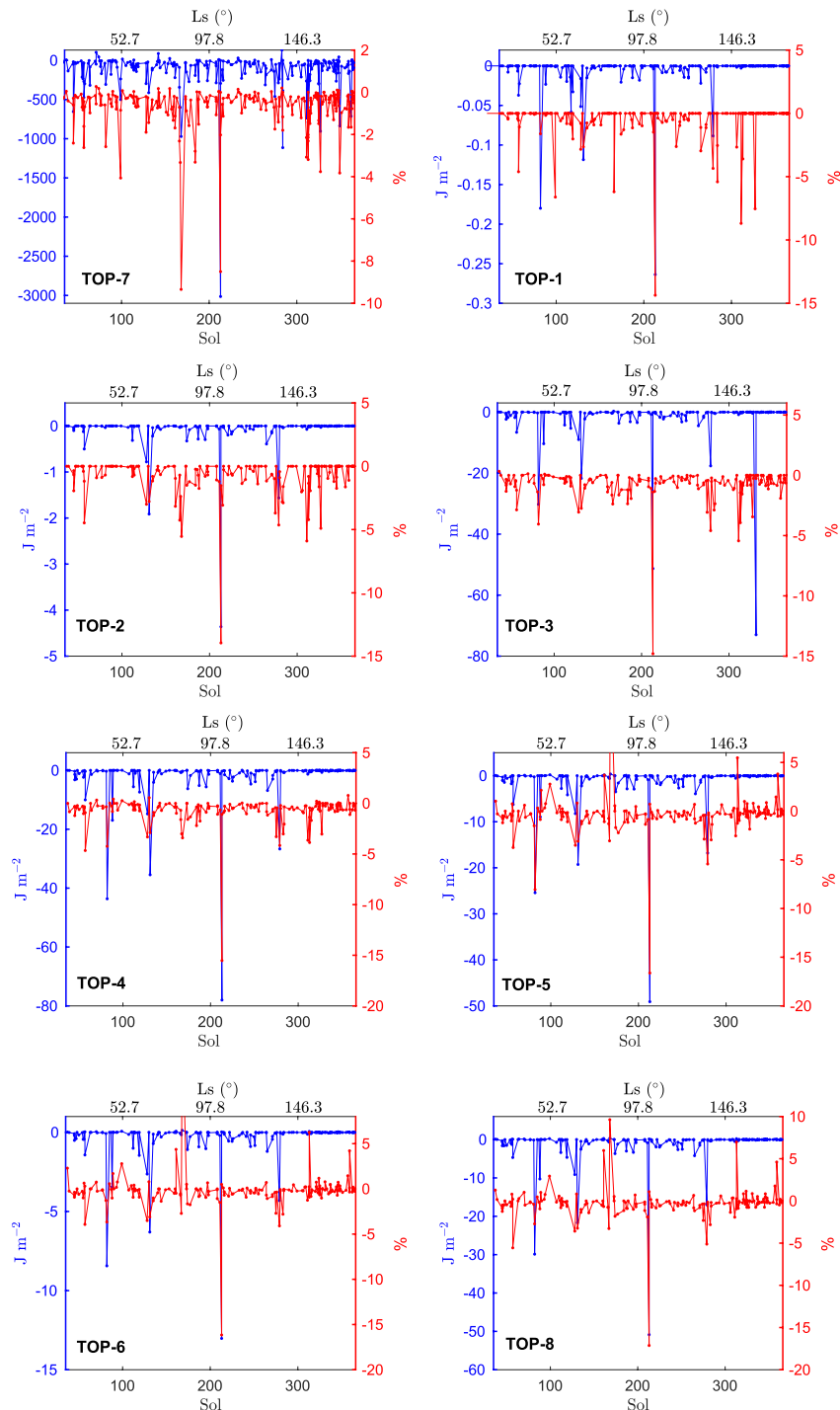
by these sensors can occur at both forward and backward scattering, and thus explains the lower number of detections registered by the UV sensors compared to the visible or near-IR sensors. Regarding the TOP-7 sensor, we found in most of the cases negative variations in IIOT with values  $\sim -0.659\%$  in average but with drops of up to  $\sim -10\%$  when the DD blocked the direct light.

In general, Figure 20 does not show a particular seasonal variation in the DD impact on the irradiance measurements. As the RDS signal drop depends on the DD dimensions, these results indicate that on average the characteristics of DD sizes are similar across the 365 sols. This is also consistent with the results given in Figure 18, which do not show a strong seasonal variation in  $d_{DD}$ . The intensity of the drops depends also on the duration of the detection, which can last from a few seconds to more than 2 min (see left panel of Figure 22). The events with longer durations are those for which the DD passed near the rover with low advection velocities and crossing all the sensor area of detection. The right panel of Figure 22 shows the correlation between the time duration of the events and the intensity of the reduction in IIOT (expressed in %). Here, we see that in general the events with longer durations presents greater drops. However, the higher drops do not correspond to the longest events (nor to the case with the largest DD diameter). Therefore, these results suggest that the magnitude of the different integrated irradiance variations depend also on other DD parameters such as the DD opacity or the distance RDS-DD.

#### 4. Discussion and Conclusions

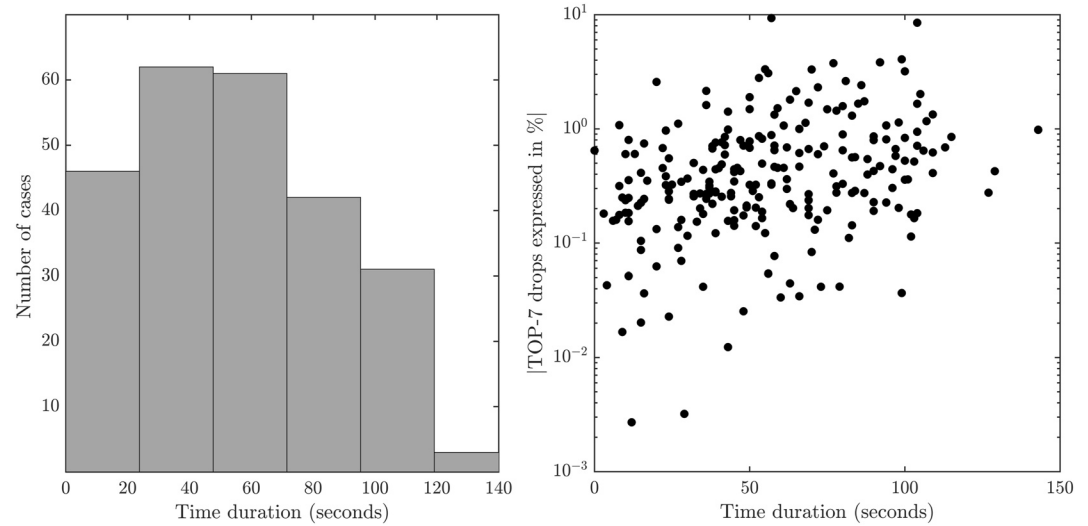
The MEDA instrument onboard Mars 2020 Perseverance rover has collected a unique set of in situ meteorological data from Jezero crater (C. E. Newman et al., 2022) and with this data set, in particular using MEDA-RDS observations, DL events such as DDs were studied for the first 365 sols of the mission (half a martian year). A principal advantage of using the MEDA-RDS data set for this study is its sampling frequency (1 Hz) and temporal coverage (see Figure 3), which allowed us to study the DD properties encompassing the full diurnal period. The period between 12:00 and 13:00 was when the maximum of detections occurred, with no other maxima found. Among all RDS detections,  $\sim 70\%$  of the cases were classified as DL events (including any DL event occurring on the surface) and  $\sim 61\%$  as DDs. For the remaining 30% of the detections, we were not able to establish the cause of the RDS signals variations.

For the whole 365-sol period, we found a DD frequency of formation between 1.3 and 3.4 DD  $\text{km}^{-2} \text{ sol}^{-1}$ , with a slight increase as a function of sol number. The DD frequency of formation at Jezero seems to lie between the values found at the Pathfinder and Spirit landing sites. From images made by Spirit's cameras, Greeley et al. (2006) and Greeley et al. (2010) derived frequencies of 51 DDs  $\text{km}^{-2} \text{ sol}^{-1}$  for Season One ( $L_s = 173^\circ\text{--}340^\circ$ , local spring and summer), 11 DDs  $\text{km}^{-2} \text{ sol}^{-1}$  for Season Two ( $L_s = 181^\circ\text{--}267^\circ$ , local spring), and 20 DDs  $\text{km}^{-2} \text{ sol}^{-1}$  for Season Three ( $L_s = 189^\circ\text{--}355^\circ$ , local spring and summer), values much greater than the DD frequency at Jezero derived in this work. Regarding the DD diameters, Greeley et al. (2010) reported median diameters of 19 m in season one, 24 m in season two, and 39 m in season three, values that are similar to those derived in Section 3.4. For the



**Figure 21.** Dust lifting radiative impact on RDS-Top measurements for the cases shown in Figure 10. Left axis represents the reductions in IIOT with respect to the case without a dust devil in  $J m^{-2}$ , while right axis in %.

Pathfinder landing site (PLS), however, a DD frequency of 0.5 DDs  $km^{-2} sol^{-1}$  (Ferri et al., 2003; Waller, 2011) was found for a period of 83 sols during the local spring and summer seasons. Although this  $\rho_{DD}$  is about 5 times smaller than the range derived in this work, Ferri et al. (2003) reported average DD diameters of  $\sim 200$  m, about 7 times larger than that obtained from the analysis of Section 3.4. For an average DD dust flux  $\bar{F}$  (amount of dust raised by a DD per unit area per time) and  $t_{DD} = 0.66 \cdot (2 \cdot r_{DD})^{0.66}$ , the total amount of dust lifted by the DDs



**Figure 22.** Histogram of the event durations (left panel) and correlation between the duration of the Top-7 drops and the integrated irradiance over the time (reduction in IIOT expressed in %).

formed in an area  $A$  and a time period  $T$  is of the order of  $\rho_{DD} \cdot A \cdot T \cdot \bar{F} \cdot \pi \bar{r}_{DD}^2 \cdot 0.66 \cdot (2 \cdot \bar{r}_{DD})^{0.66}$ , where the product of the first three terms expresses the total number of DDs and the product of the rest of the terms expresses the amount of dust lifted per DD (in units of mass). If we assume the same average DD dust flux at the two locations (e.g., we use the mean value of  $2.10^{-5} \text{ kg m}^{-2} \text{ s}^{-1}$  derived in Greeley et al. (2006) for Gusev crater), then the ratio between the dust raised by DDs at PLS and Jezero is of the order of  $\frac{0.5 \text{ km}^{-2} \text{ sol}^{-1}}{\rho_{DD, \text{Thiswork}}} \times \left( \frac{200 \text{ m}}{\bar{r}_{DD, \text{Thiswork}}} \right)^{2.66} \sim 30$ . That is to say, even if  $\rho_{DD}$  is larger at Jezero, the larger  $\bar{r}_{DD}$  at PLS results in a greater amount of dust lifted by DDs. Therefore, the product  $\rho_{DD} \times \bar{r}_{DD}^{2.66}$  is a better metric than  $\rho_{DD}$  to compare two locations in terms of the amount of dust raised by DDs (as long as the  $\bar{r}_{DD}$  at the two locations are significantly different).

Regarding InSight landing site (ILS), Reiss et al. (2016) and Perrin et al. (2020) derived from the DD tracks (DDT) imaged with orbiters the seasonal variation of the DDT frequencies. In particular, they found for midspring a frequency of  $\sim 0.05 \text{ DDT sol}^{-1} \text{ km}^{-2}$ , following by a major decrease in late spring. These results indicate DD frequencies at ILS much lower than that estimated for Jezero and explain the lack of visual DD detections by the lander (Jackson et al., 2021; Spiga et al., 2021). In terms of dust lifted by DDs, Reiss et al. (2016) reported DD diameters  $< 10 \text{ m}$ , resulting in  $\rho_{DD} \times \bar{r}_{DD}^{2.66}$  values by about  $\sim 10^{-3}$  smaller than that estimated in this work. Hence, these different results, along with other works (e.g., L. K. Fenton & Lorenz, 2015; Fisher et al., 2005), indicate notably place-to-place and year-to-year variations in DD frequency.

Although the DD frequency was well constrained with MEDA-RDS observations, information on the DD diameter characteristics, migration direction, and advection velocity is limited to the cases for which the DD blocked the direct light or to events on which we have different Lat sensors detections. For these particular cases we found the following: (a) an average, maximum, and minimum diameters of 29 m,  $132 \pm 63.4 \text{ m}$ , and  $5.6 \pm 5.5 \text{ m}$  and without apparent seasonal changes; (b) DD migration directions in agreement with MEDA wind data. A constraint on the minimum DD height was also derived from Top detections. For the whole period, we estimated an average minimum DD height of 231 m and a maximum of 872 m. The period between sols 125 and 225 ( $L_s = 64^\circ\text{--}109^\circ$ ) shows greater minimum DD height which may be related with variations in the planetary boundary layer (L. K. Fenton & Lorenz, 2015). From the average diameter and  $t_{DD} = 0.66 \times (2 \times r_{DD})^{0.66}$  (R. Lorenz, 2013), we derived an average DD lifetime of about 6 min.

The differences in DD dimension, as well as other parameter such the DD height, impacted the irradiance levels measured by RDS (see Figure 21). In all the DD cases, the presence of a DD near the rover resulted in a decrease in the UV fluxes, in contrast to the visible and near-IR sensors for which both increments and decreases with respect to the background irradiance were observed. Expressed in terms of the irradiance integrated over the time duration of the event (IIOT), we obtained an average value of  $\sim -0.659\%$  for TOP-7 sensor (190–1,200 nm).



However, the events display a wide range of IIOT values that correspond to the different detection scenarios (DD blocking the direct light or DD passing at different distance from the rover) and DD properties (advection velocity, dimensions, opacity, and lifetime).

### Appendix A: Estimation of the Dust Devil Opacity From RDS Top Sensor Observations

For the DD detection cases that involved a blocking of direct light, and the DD was at a distance such that the scattered light received by the Top sensors was practically unaffected by the DD, a direct estimation of  $\tau_{DD}$  is possible. The intensities measured by a Top sensor before ( $I_{TOTAL,1}$ ) and during ( $I_{TOTAL,2}$ ) the direct light-blocking are given by the following equations:

$$I_{TOTAL,1} = I_{scatt,1} + C \cdot FOV(SZA, PHI0) \cdot e^{-\tau_{dust}/SZA} \quad (A1)$$

$$I_{TOTAL,2} = I_{scatt,2} + C \cdot FOV(SZA, PHI0) \cdot e^{-\tau_{dust}/SZA} \cdot e^{-\tau_{DD}} \quad (A2)$$

where  $\tau_{dust}$  is the column dust opacity,  $I_{scatt,i}$  is the scattered light contribution (produced by the DD and the background dust), and  $C$  is the solar flux at the top of the atmosphere over the sensor wavelength range, which is constant for each sensor. The second term on the right side of Equations A1 and A2 represents the direct light contribution to the total intensity (see Toledo et al. (2016) for more details). If the DD is at a far distance from RDS, we can assume that most of the scattered light received by the Top sensors is due to the background dust, and thus  $I_{scatt,1} = I_{scatt,2}$ . An example of such events is the one shown in Figure 4 (sol 21); three Lat sensors detect the DD but the Top channels do not see it up to the moment when the direct light is blocked. Therefore, in these cases we can combine Equations A1 and A2 as follows:

$$e^{-\tau_{DD}} = 1 - \frac{I_{TOTAL,1} - I_{TOTAL,2}}{C \cdot FOV(SZA, PHI0) \cdot e^{-\tau_{dust}/SZA}} \quad (A3)$$

For a known dust opacity  $\tau_{dust}$ , the DD opacity along the line of sight  $\tau_{DD}$  can be estimated from Equation A3, as  $(I_{TOTAL,1} - I_{TOTAL,2})$  is calculated from the measurements made by the sensor that detect the direct light-blocking. Note that for this calculation of  $\tau_{DD}$ , we do not make use of any RT simulations.

### Appendix B: Geometric Model

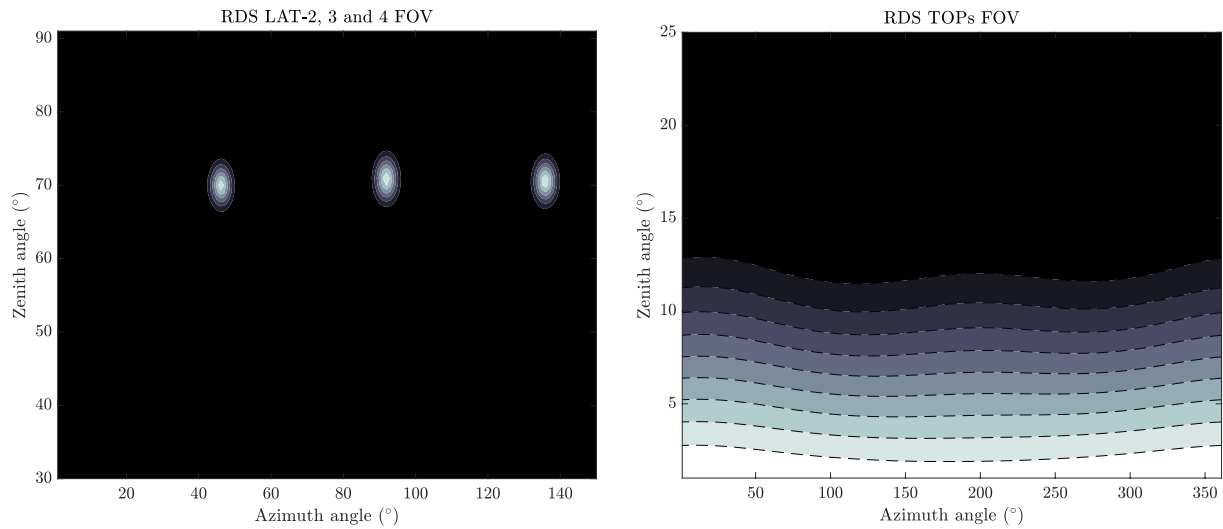
For a given DD detected by any of RDS sensors and for known values of  $d_{DD}$ ,  $h_{DD}$ , and the distance between RDS and DD, we can compute the % of the sensor FOV that is covered by the DD. For Lat sensors and assuming a cylinder shape, this % can be approximated by the following equation:

$$P = 100 \times \frac{C \cdot (A - 15^\circ) \times B}{A_{sensor}} \quad (B1)$$

where  $A_{sensor}$  represents the sensor-FOV area (see Figure B1) in the zenith-azimuth space (e.g., for Lat sensors, we have  $A_{sensor} = \pi \times (5^\circ)^2$ ) and

$$C = \begin{cases} 0 & \text{for } (d - r_{DD}) \cdot \tan(15^\circ) > h_{DD} \\ 1 & \text{for } (d - r_{DD}) \cdot \tan(15^\circ) \leq h_{DD} \end{cases} \quad (B2)$$

$$A = \begin{cases} 25^\circ & \text{for } (d - r_{DD}) \cdot \tan(25^\circ) < h_{DD} \\ \arctg\left(\frac{h_{DD}}{d - r_{DD}}\right) & \text{for } (d - r_{DD}) \cdot \tan(25^\circ) \geq h_{DD} \end{cases} \quad (B3)$$



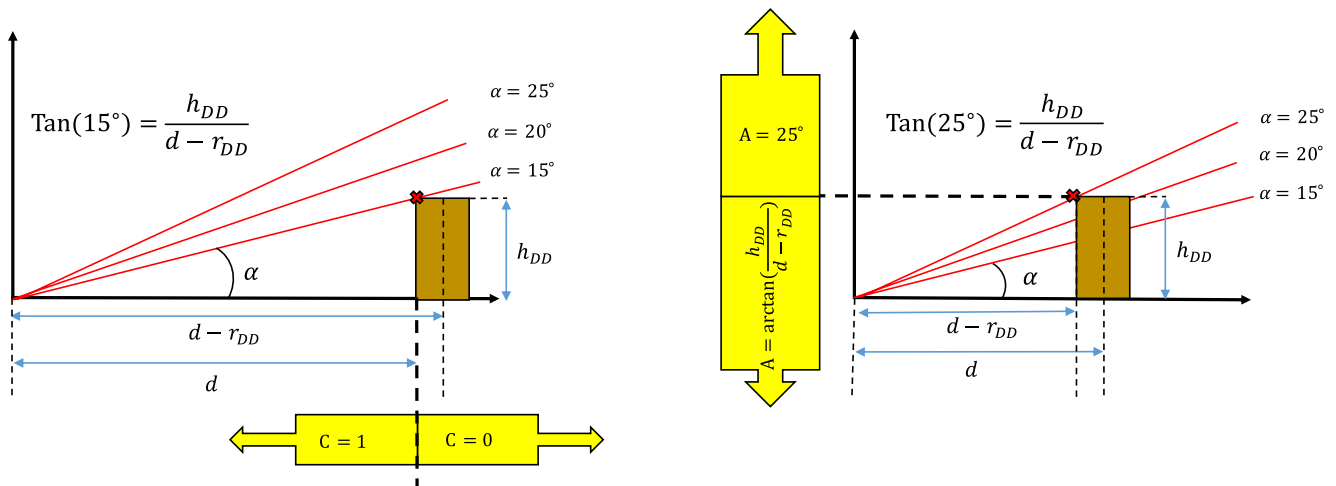
**Figure B1.** Measured RDS Lat (left) and Top (right) sensors field of view. White and black areas correspond to 100% and 0% of transmission, respectively. For Top sensors (except for Top 7), most light is collected for zenith angles between 0° and 15°.

$$B = \begin{cases} 2 \cdot \arctg\left(\frac{r_{DD}}{d}\right) & \text{for } \arctg\left(\frac{r_{DD}}{d}\right) < 5^\circ \\ 10^\circ & \text{for } \arctg\left(\frac{r_{DD}}{d}\right) \geq 5^\circ \end{cases} \quad (\text{B4})$$

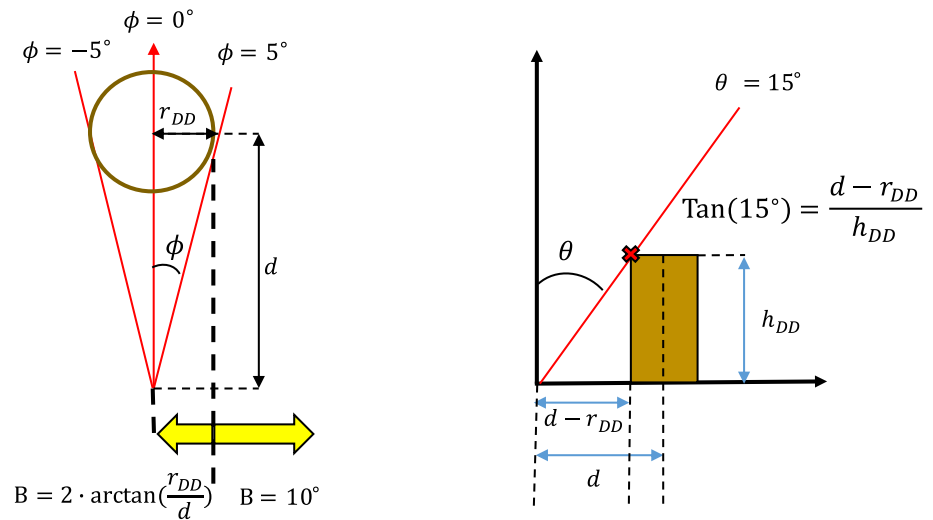
For given values of  $h_{DD}$ ,  $r_{DD}$ , and  $d$ , the term  $C$  in Equation B2 establishes whether the DD is high enough to intersect the LAT-sensor FOV (assuming the DD is in front of the sensor). Thus, if  $C = 1$  the DD projection over the sensor FOV is approximated by the product between  $(A-15^\circ)$  and  $B$ , which represents the FOV zenith range and azimuth range covered by the DD. The geometric interpretation of terms  $A$  and  $B$  are illustrated in right panel of Figure B2 and left panel of Figure B3.

For Top sensors the % of the FOV covered by the DD is approximated by the following equation:

$$P = 100 \times \frac{\left(15^\circ - \arctg\left(\frac{d-r_{DD}}{h_{DD}}\right)\right) \times 2 \cdot \arctg\left(\frac{r_{DD}}{d}\right)}{A_{\text{sensor}}} \quad (\text{B5})$$



**Figure B2.** Left) Diagram showing the maximum distance  $d^*$  at which a dust devil (DD) (with radius  $r_{DD}$  and height  $h_{DD}$ ) localized in front of a Lat sensor intersects with the field of view (FOV). For distances  $\leq d^*$  the term  $C$  of Equation B1 is equal to 1, while for distances  $> d^*$   $C = 0$ . Right) Maximum elevation angle ( $\alpha = 90^\circ - \theta$ , being  $\theta$  the zenith angle) in the projection of the DD over the sensor FOV. As Lat sensors point at  $\alpha = 20^\circ \pm 5^\circ$ , the maximum value of  $A$  in Equation B3 is  $25^\circ$ .

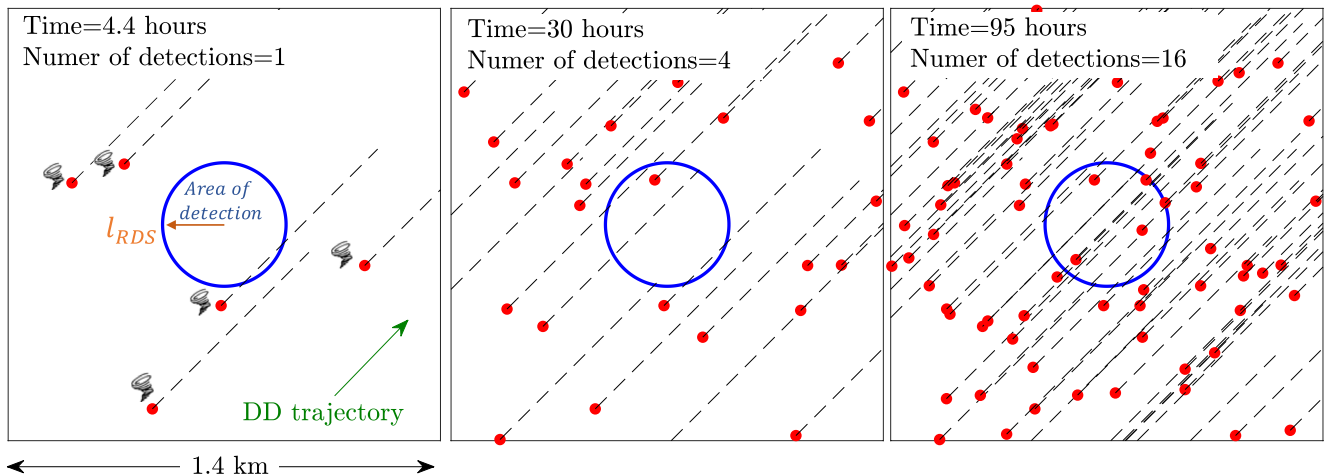


**Figure B3.** Left) Range of field of view (FOV) azimuth angles ( $\phi$ ) covered by a dust devil (DD) (with radius  $r_{DD}$  and height  $h_{DD}$ ) localized in front of one the Lat sensor at a distance  $d$ . Right) Diagram showing the intersection between the DD and the Top sensor FOV.

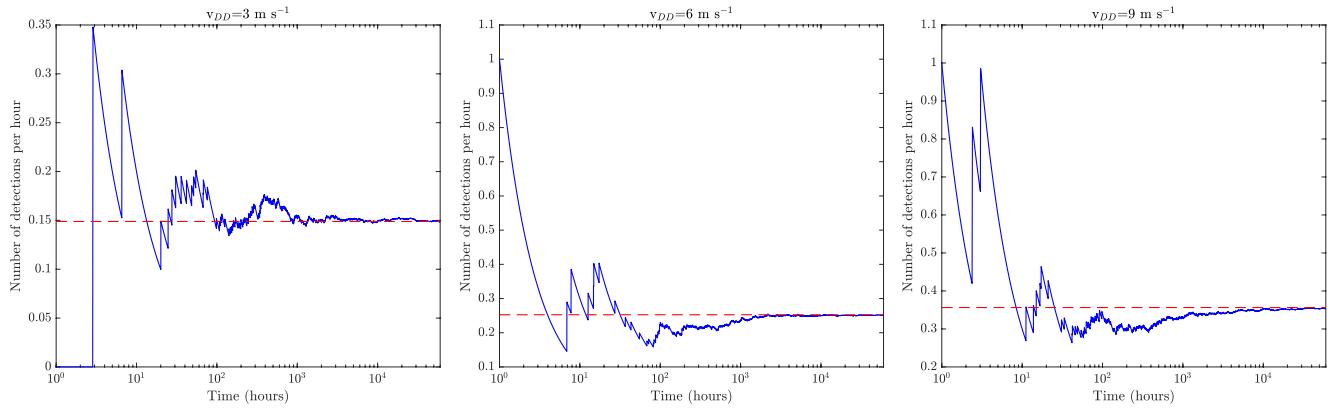
where  $P = 0$  for  $h_{DD} < d/\tan(15^\circ)$  (no intersection between FOV and DD). The two terms of the right side of Equation B5 give the ranges of zenith and azimuth angles of the FOV covered by the DD (see right panel of Figure B3). Therefore, by using Equation B1 and B5, we can easily evaluate the variation of  $P$  with the DD dimensions and the distance between the DD and RDS.

### Appendix C: Dust Devil Frequency of Occurrence From MC

For a given DD frequency of formation  $\rho_{DD}$ , the total number of DDs ( $N_{DD}$ ) formed in a given area  $A_{max} = \pi \cdot d_{max}^2$  and time period  $\Delta t$  is given by  $N_{DD} = \rho_{DD} \cdot A_{max} \cdot \Delta t$ . The % of  $N_{DD}$  detected with RDS is given by (a) the number of DD that crosses the RDS area of detection, given by  $A_{RDS} = \pi \cdot l_{RDS}^2$  (for Top channels) and (b) the cases that block the sun direct light. In the model each DD of the total  $N_{DD}$  is formed within the area  $A_{max}$ , whose coordinates are given by Equation 3. Subsequently, the DDs travels a distance  $l_{DD} \cdot v_{DD}$  following a straight line (defined by the migration direction) that may or may not cross  $A_{RDS}$  (see Figure C1). Direct light-blocking events occur when DD trajectory crosses the sun azimuth angle  $\text{PHIO}$  and  $h_{DD} \geq d/\tan(\text{SZA})$ , where  $d$  is the distance between the DD and RDS when the DD azimuth angle =  $\text{PHIO}$ .



**Figure C1.** Schematic of the evolution of RDS detections for a constant dust devil (DD) frequency  $\rho_{DD} = 0.36 \text{ DD km}^{-2} \text{ hr}^{-1}$  and a DD advection velocity of  $3 \text{ m s}^{-1}$ . The blue circle indicates the RDS area of detection  $A_{DD}$ , while the red dots along with the black dashed lines represent the initial DD location and its trajectory, respectively. If a DD crosses  $A_{DD}$  and also blocks the sun direct light, only one detection is counted in the model.



**Figure C2.** Temporal evolution of RDS detections per hour simulated with MC (blue solid line) and Equation 4 (red dashed line) for a constant dust devil (DD) frequency  $\rho_{DD} = 0.36 \text{ DD km}^{-1} \text{ hr}^{-1}$ , and DD advection velocities of  $3 \text{ m s}^{-1}$  (left panel),  $6 \text{ m s}^{-1}$  (middle panel), and  $9 \text{ m s}^{-1}$  (right panel). We see that a steady value is not achieved with MC until the number of DDs  $N_{DD}$  does not reach a certain threshold, which mainly depends on  $\rho_{DD}$ ,  $v_{DD}$ ,  $A_{DD}$ , and  $t_{DD}$ .

Figure C2 shows the temporal evolution of RDS detections with time simulated with MC and Equation 4 for a constant DD frequency and three different advection velocities. Although a steady value is not achieved after several hours (or number of DD launched in  $A_{max}$ ), we observe that MC and Equation 4 provide similar results. Note that as  $v_{DD}$  and  $t_{DD}$  increase, the  $A_{max}$  required for simulating the RDS detections per time becomes larger, and thus  $N_{DD}$  as well. Indeed,  $d_{max}$  defining the DD area of formation should be greater than  $l_{RDS} + v_{DD} \cdot t_{DD}$  ( $l_{RDS}$  computed from the results shown in Section 2.4). For the Top sensors with a simple area of detection the use of Equation 4 to compute  $\rho_{DD}$  presents greater advantages over MC. However, for sensors with more complicated areas of detections (e.g., Lat sensors) or combining sensors with different FOVs, the use of MC may be much simpler.

#### Appendix D: Errors in the Estimation of $\rho_{DD}$

The largest uncertainties in the calculation of  $\rho_{DD}$  are introduced by the DD parameters  $r_{DD}$ ,  $h_{DD}$ , and  $t_{DD}$ , which are unknown and have an impact on the sensor limit of detection, the DD direct light-blocking cases and the increase in the effective area (Equation 4). From RT simulations similar to those shown in Figure 8, we can evaluate the variation in  $l_{RDS}$ , and so in  $\rho_{DD}$ , when we vary the DD parameters within the expected range of values on Mars. We first tested the variations in  $\rho_{DD}$  when the average DD height is varied from  $h = 400\text{--}1,400 \text{ m}$ , range selected based on previous works (e.g., Cantor et al., 2006; L. K. Fenton & Lorenz, 2015; Fisher et al., 2005). In this case  $r_{DD}$  and  $t_{DD}$  were fixed constant:  $r_{DD} = 14.5 \text{ m}$  (average value derived in Section 3.4) and  $t_{DD} = 0.66 \cdot (2 \cdot r_{DD})^{0.66}$ . For each channel, we computed  $l_{RDS}$  for the parameter sets ( $h_{DD} = 400 \text{ m}, r_{DD} = 14.5 \text{ m}, t_{DD} = 6 \text{ min}$ ) and ( $h_{DD} = 1,400 \text{ m}, r_{DD} = 14.5 \text{ m}, t_{DD} = 6 \text{ min}$ ), and then  $\rho_{DD}$  from Equations 4 and 5. This provides a maximum value of  $\rho_{DD}$  (for  $h_{DD} = 400 \text{ m}$ ) and a minimum (for  $h_{DD} = 1,400 \text{ m}$ ). Subsequently, a similar analysis was performed but for the other DD parameters,  $r_{DD}$  and  $t_{DD}$ . In particular, we varied  $r_{DD}$ , and so  $t_{DD}$ , from  $25 \text{ m}$  (value used in the simulations shown in Figure 12) to  $14.5 \text{ m}$ , which is the average radius estimated in Section 3.4 ( $h_{DD}$  was fixed to a constant value of  $800 \text{ m}$ ). In this case, the maximum and minimum  $\rho_{DD}$  values were within the range estimated for  $h_{DD} = 400$  and  $1,400 \text{ m}$ , and thus it is the  $h_{DD}$ , the parameter selected for defining the final errors in  $\rho_{DD}$ . Similar tests were done for the DD opacity ( $\tau_{DD}$ ). As indicated in Section 2.4, only in a few cases, we could estimate  $\tau_{DD}$  from the observations. By using the DD opacity derived for the case on sol 21 as reference, we varied the value of  $\tau_{DD}$  as we did for  $r_{DD}$ ,  $h_{DD}$ , and  $t_{DD}$ . We found that by changing  $r_{DD}$  by a 50%, the range of  $\rho_{DD}$  values is, as it was for  $r_{DD}$ , within the errors derived from  $h_{DD}$ .

In summary, the procedure to compute the errors in  $\rho_{DD}$  is as follows: (a) we first compute for each DD detection the limit of detection  $l_{RDS}$  for  $r_{DD} = 14.5 \text{ m}$  and  $h_{DD} = 400 \text{ m}$ ; (b) subsequently,  $\rho_{DD}$  lower limit is computed from  $l_{RDS}$  derived in previous step and using Equations 4 and 5 (for  $h_{DD} = 400 \text{ m}, t_{DD} = 0.66 \times (29)^{0.66}$ ); and (c)  $\rho_{DD}$  upper limit is obtained by repeating the steps (a) and (b) but for  $h_{DD} = 1,400 \text{ m}$ . This procedure is applied to the detections performed by Top-4 ( $\Delta\rho_{DD}^{Top4}$ ) and Top-8 ( $\Delta\rho_{DD}^{Top8}$ ), and then the final error is given by the range that covers both  $\Delta\rho_{DD}^{Top4}$  and  $\Delta\rho_{DD}^{Top8}$  (see black dashed lines in Figure 15).

## Data Availability Statement

All perseverance data used in this study are publicly available via the Planetary Data System (J. M. Maki, 2021; Rodriguez-Manfredi & de la Torre Juarez, 2021). The radiative transfer simulations, dust devil retrievals, and derived data of Figures 8–10, 12, 14, 15, 17–19, 21, 22, and C2 are available in an archive located at Toledo (2022), version 2.

## Acknowledgments

This work has been funded by the Spanish Ministry of Economy and Competitiveness, through the projects no. ESP2014-54256-C4-1-R (also -2-R, -3-R and -4-R); Ministry of Science, Innovation and Universities, projects no. ESP2016-79612-C3-1-R (also -2-R and -3-R); Ministry of Science and Innovation/State Agency of Research (10.13039/501100011033), projects no. ESP2016-80320-C2-1-R, RTI2018-098728-B-C31 (also -C32 and -C33), RTI2018-099825-B-C31. RH and ASL were supported by the Spanish project PID2019-109467GB-I00 funded by MCIN/AEI/10.13039/501100011033 and by Grupos Gobierno Vasco IT1742-22. The US co-authors performed their work under sponsorship from NASA's Mars 2020 project, from the Game Changing Development programme within the Space Technology Mission Directorate and from the Human Exploration and Operations Directorate. Part of this research was carried out at the Jet Propulsion Laboratory, California Institute of Technology, under a contract with the National Aeronautics and Space Administration (80NM0018D0004). G.M. acknowledges JPL funding from USRA Contract Number 1638782. ML is supported by contract 15-712 from Arizona State University and 1607215 from Caltech-JPL.

## References

- Apestigue, V., Gonzalo, A., Jiménez, J. J., Boland, J., Lemmon, M., de Mingo, J. R., et al. (2022). Radiation and dust sensor for Mars environmental dynamic analyzer onboard M2020 rover. *Sensors*, 22(8), 2907. <https://doi.org/10.3390/s22082907>
- Arruego, I., Apéstigue, V., Jiménez-Martín, J., Martínez-Oter, J., Álvarez-Ríos, F., González-Guerrero, M., et al. (2017). Dreams-sis: The solar irradiance sensor on-board the exomars 2016 lander. *Advances in Space Research*, 60(1), 103–120. <https://doi.org/10.1016/j.asr.2017.04.002>
- Bagnold, R. A. (2012). *The physics of blown sand and desert dunes*. Courier Corporation.
- Balme, M., & Greeley, R. (2006). Dust devils on Earth and Mars. *Reviews of Geophysics*, 44(3), RG3003. <https://doi.org/10.1029/2005rg000188>
- Balme, M. R., Whelley, P. L., & Greeley, R. (2003). Mars: Dust devil track survey in argyre planitia and Hellas basin. *Journal of Geophysical Research*, 108(E8), 5086. <https://doi.org/10.1029/2003je002096>
- Banfield, D., Spiga, A., Newman, C., Forget, F., Lemmon, M., Lorenz, R., et al. (2020). The atmosphere of Mars as observed by insight. *Nature Geoscience*, 13(3), 190–198. <https://doi.org/10.1038/s41561-020-0534-0>
- Basu, S., Richardson, M. I., & Wilson, R. J. (2004). Simulation of the Martian dust cycle with the GFDL Mars GCM. *Journal of Geophysical Research*, 109(E11), E11006. <https://doi.org/10.1029/2004je002243>
- Calef, F., Soliman, T., Roberts, J., Chung, A., Abarca, H., & Dahl, L. (2021). NASA ammos multi-mission geographic information system (MMGIS) version 2.0: Updates and mission operations. *LPI Contribution*, 2549, 7061.
- Cantor, B. A., Kanak, K. M., & Edgett, K. S. (2006). Mars orbiter camera observations of Martian dust devils and their tracks (September 1997 to January 2006) and evaluation of theoretical vortex models. *Journal of Geophysical Research*, 111(E12), E12002. <https://doi.org/10.1029/2006je002700>
- Community, B. O. (2018). *Blender—A 3D modelling and rendering package*. Blender Foundation.
- Cushing, G. E., Titus, T. N., & Christensen, P. R. (2005). Themis vis and ir observations of a high-altitude Martian dust devil. *Geophysical Research Letters*, 32(23), L23202. <https://doi.org/10.1029/2005gl024478>
- Daubar, I., Ojha, L., Chojnacki, M., Golombek, M., Lorenz, R., Wray, J., & Lewis, K. (2018). Lifetime of a dust devil track and dust deposition rate in Gusev crater. In *49th annual lunar and planetary science conference* (p. 1730).
- Eillehoj, M., Gunnlaugsson, H., Taylor, P., Kahanpää, H., Bean, K., Cantor, B., et al. (2010). Convective vortices and dust devils at the phoenix Mars mission landing site. *Journal of Geophysical Research*, 115(E4), E00E16. <https://doi.org/10.1029/2009je003413>
- Farley, K. A., Williford, K. H., Stack, K. M., Bhartia, R., Chen, A., de la Torre, M., et al. (2020). Mars 2020 mission overview. *Space Science Reviews*, 216(8), 1–41. <https://doi.org/10.1007/s11214-020-00762-y>
- Fenton, L., Reiss, D., Lemmon, M., Marticorena, B., Lewis, S., & Cantor, B. (2016). Orbital observations of dust lofted by daytime convective turbulence. *Space Science Reviews*, 203(1), 89–142. <https://doi.org/10.1007/s11214-016-0243-6>
- Fenton, L. K., & Lorenz, R. (2015). Dust devil height and spacing with relation to the Martian planetary boundary layer thickness. *Icarus*, 260, 246–262. <https://doi.org/10.1016/j.icarus.2015.07.028>
- Ferguson, R., Hare, T., Mayer, D., Galuszka, D., Redding, B., Smith, E., et al. (2020). Mars 2020 terrain relative navigation flight product generation: Digital terrain model and orthorectified image mosaic. In *Lunar and planetary science conference*.
- Ferri, F., Smith, P. H., Lemmon, M., & Rennó, N. O. (2003). Dust devils as observed by Mars pathfinder. *Journal of Geophysical Research*, 108(E12), 5133. <https://doi.org/10.1029/2000je001421>
- Fisher, J. A., Richardson, M. I., Newman, C. E., Szwast, M. A., Graf, C., Basu, S., et al. (2005). A survey of Martian dust devil activity using Mars global surveyor Mars orbiter camera images. *Journal of Geophysical Research*, 110(E3), E03004. <https://doi.org/10.1029/2003je002165>
- Gómez-Elvira, J., Armiens, C., Castañer, L., Domínguez, M., Genzer, M., Gómez, F., et al. (2012). Rems: The environmental sensor suite for the Mars Science Laboratory rover. *Space Science Reviews*, 170(1), 583–640. <https://doi.org/10.1007/s11214-012-9921-1>
- Greeley, R., Balme, M. R., Iversen, J. D., Metzger, S., Mickelson, R., Phoreman, J., & White, B. (2003). Martian dust devils: Laboratory simulations of particle threshold. *Journal of Geophysical Research*, 108(E5), 5041. <https://doi.org/10.1029/2002je001987>
- Greeley, R., Waller, D. A., Cabrol, N. A., Landis, G. A., Lemmon, M. T., Neakrase, L. D., et al. (2010). Gusev crater, Mars: Observations of three dust devil seasons. *Journal of Geophysical Research*, 115(E7), E00F02. <https://doi.org/10.1029/2010je003608>
- Greeley, R., Whelley, P. L., Arvidson, R. E., Cabrol, N. A., Foley, D. J., Franklin, B. J., et al. (2006). Active dust devils in Gusev crater, Mars: Observations from the Mars exploration rover spirit. *Journal of Geophysical Research*, 111(E12), E12S09. <https://doi.org/10.1029/2006je002743>
- Haberle, R. M., Murphy, J. R., & Schaeffer, J. (2003). Orbital change experiments with a Mars general circulation model. *Icarus*, 161(1), 66–89. [https://doi.org/10.1016/s0019-1035\(02\)00017-9](https://doi.org/10.1016/s0019-1035(02)00017-9)
- Hueso, R., Newman, C., del Rio-Gaztelurrutia, T., Munguira, A., Sánchez-Lavega, A., Toledo, D., et al. (2022). Convective vortices and dust devils detected and characterized by Mars 2020. *Earth and Space Science Open Archive*, 32. <https://doi.org/10.1002/essoar.10512158.1>
- Jackson, B. (2022). Vortices and dust devils as observed by the Mars environmental dynamics analyzer instruments on board the Mars 2020 perseverance rover. *The Planetary Science Journal*, 3(1), 20. <https://doi.org/10.3847/psj/ac4586>
- Jackson, B., Crevier, J., Szurgot, M., Battin, R., Perrin, C., & Rodriguez, S. (2021). Inferring vortex and dust devil statistics from insight. *The Planetary Science Journal*, 2(5), 206. <https://doi.org/10.3847/psj/ac260d>
- Kahanpää, H., Newman, C., Moores, J., Zorzano, M.-P., Martín-Torres, J., Navarro, S., et al. (2016). Convective vortices and dust devils at the MSL landing site: Annual variability. *Journal of Geophysical Research: Planets*, 121(8), 1514–1549. <https://doi.org/10.1002/2016je005027>
- Kahanpää, H., & Viúdez-Moreiras, D. (2021). Modelling Martian dust devils using in situ wind, pressure, and UV radiation measurements by Mars Science Laboratory. *Icarus*, 359, 114207. <https://doi.org/10.1016/j.icarus.2020.114207>
- Kahre, M. A., Murphy, J. R., & Haberle, R. M. (2006). Modeling the Martian dust cycle and surface dust reservoirs with the NASA Ames general circulation model. *Journal of Geophysical Research*, 111(E6), E06008. <https://doi.org/10.1029/2005je002588>
- Kok, J. F., Parteli, E. J., Michaels, T. L., & Karam, D. B. (2012). The physics of wind-blown sand and dust. *Reports on Progress in Physics*, 75(10), 106901. <https://doi.org/10.1088/0034-4885/75/10/106901>

- Lemmon, M., Smith, M. D., Viudez-Moreiras, D., de la Torre-Juarez, M., Vicente-Retortillo, A., Munguira, A., et al. (2022). Dust, sand, and winds within an active Martian storm in Jezero crater. *Geophysical Research Letters*, *49*(17), e2022GL100126. <https://doi.org/10.1029/2022gl100126>
- Lorenz, R. (2013a). The longevity and aspect ratio of dust devils: Effects on detection efficiencies and comparison of landed and orbital imaging at Mars. *Icarus*, *226*(1), 964–970. <https://doi.org/10.1016/j.icarus.2013.06.031>
- Lorenz, R. D. (2013b). Irregular dust devil pressure drops on Earth and Mars: Effect of cycloidal tracks. *Planetary and Space Science*, *76*, 96–103. <https://doi.org/10.1016/j.pss.2013.01.001>
- Lorenz, R. D. (2016). Heuristic estimation of dust devil vortex parameters and trajectories from single-station meteorological observations: Application to insight at Mars. *Icarus*, *271*, 326–337. <https://doi.org/10.1016/j.icarus.2016.02.001>
- Lorenz, R. D., & Jackson, B. K. (2015). Dust devils and dustless vortices on a desert playa observed with surface pressure and solar flux logging. *GeoResJ*, *5*, 1–11. <https://doi.org/10.1016/j.grj.2014.11.002>
- Lorenz, R. D., Lemmon, M. T., & Maki, J. (2021). First Mars year of observations with the insight solar arrays: Winds, dust devil shadows, and dust accumulation. *Icarus*, *364*, 114468. <https://doi.org/10.1016/j.icarus.2021.114468>
- Maki, J., Bell, J., III, Herkenhoff, K. E., Squyres, S., Kiely, A., Klimesh, M., et al. (2003). Mars exploration rover engineering cameras. *Journal of Geophysical Research*, *108*(E12), 8071. <https://doi.org/10.1029/2003je002077>
- Maki, J., Thiessen, D., Pourangi, A., Kobzeff, P., Litwin, T., Scherr, L., et al. (2012). The Mars Science Laboratory engineering cameras. *Space Science Reviews*, *170*(1), 77–93. <https://doi.org/10.1007/s11214-012-9882-4>
- Maki, J. M. (2021). Calibrated data products for the Mars 2020 perseverance rover navigation cameras. *PDS Imaging Node*, *10*. <https://doi.org/10.17189/lyvkm-rx37>
- Metzger, S. M. (1999). *Dust devils as Aeolian transport mechanisms in southern Nevada and the Mars pathfinder landing site*. University of Nevada.
- Metzger, S. M., Carr, J. R., Johnson, J. R., Parker, T. J., & Lemmon, M. T. (2000). Techniques for identifying dust devils in Mars pathfinder images. *IEEE Transactions on Geoscience and Remote Sensing*, *38*(2), 870–876. <https://doi.org/10.1109/36.842015>
- Moore, J. E., Lemmon, M. T., Kahanpää, H., Rafkin, S. C., Francis, R., Pla-Garcia, J., et al. (2015). Observational evidence of a suppressed planetary boundary layer in northern gale crater, Mars as seen by the Navcam instrument onboard the Mars Science Laboratory rover. *Icarus*, *249*, 129–142. <https://doi.org/10.1016/j.icarus.2014.09.020>
- Murphy, J. R., & Nelli, S. (2002). Mars pathfinder convective vortices: Frequency of occurrence. *Geophysical Research Letters*, *29*(23), 18–21. <https://doi.org/10.1029/2002gl015214>
- Newman, C., De La Torre Juarez, M., Pla-García, J., Wilson, R., Lewis, S., Neary, L., et al. (2021). Multi-model meteorological and Aeolian predictions for Mars 2020 and the Jezero crater region. *Space Science Reviews*, *217*(1), 1–68. <https://doi.org/10.1007/s11214-020-00788-2>
- Newman, C. E., Hueso, R., Lemmon, M. T., Munguira, A., Vicente-Retortillo, Á., Apestigue, V., et al. (2022). The dynamic atmospheric and Aeolian environment of Jezero crater, Mars. *Science Advances*, *8*(21), eabn3783.
- Newman, C. E., Kahanpää, H., Richardson, M., Martínez, G. M., Vicente-Retortillo, A., & Lemmon, M. T. (2019). Marswrf convective vortex and dust devil predictions for gale crater over 3 Mars years and comparison with MSL-REMS observations. *Journal of Geophysical Research: Planets*, *124*(12), 3442–3468. <https://doi.org/10.1029/2019je006082>
- Newman, C. E., Lewis, S. R., Read, P. L., & Forget, F. (2002). Modeling the Martian dust cycle 2. Multiannual radiatively active dust transport simulations. *Journal of Geophysical Research*, *107*(E12), 7–1. <https://doi.org/10.1029/2002je001920>
- Ordóñez-Etxeberria, I., Hueso, R., & Sánchez-Lavega, A. (2018). A systematic search of sudden pressure drops on gale crater during two Martian years derived from MSL/REMS data. *Icarus*, *299*, 308–330. <https://doi.org/10.1016/j.icarus.2017.07.032>
- Ordóñez-Etxeberria, I., Hueso, R., & Sánchez-Lavega, A. (2020). Strong increase in dust devil activity at gale crater on the third year of the MSL mission and suppression during the 2018 global dust storm. *Icarus*, *347*, 113814. <https://doi.org/10.1016/j.icarus.2020.113814>
- Perrin, C., Rodríguez, S., Jacob, A., Lucas, A., Spiga, A., Murdoch, N., et al. (2020). Monitoring of dust devil tracks around the insight landing site, Mars, and comparison with in situ atmospheric data. *Geophysical Research Letters*, *47*(10), e2020GL087234. <https://doi.org/10.1029/2020gl087234>
- Pyrzak, G., Puncel, R., Vona, M. A., & Lopez-Roig, R. (2022). The Mars 2020 ground data system architecture. In *2022 IEEE aerospace conference (aero)* (pp. 1–20).
- Read, P. L., & Lewis, S. R. (2004). *The Martian climate Revisited: Atmosphere and environment of a desert planet*. Springer Science & Business Media.
- Reiss, D., Fenton, L., Neakrase, L., Zimmerman, M., Statella, T., Whelley, P., et al. (2016). Dust devil tracks. *Space Science Reviews*, *203*(1), 143–181. <https://doi.org/10.1007/s11214-016-0308-6>
- Reiss, D., Hoekzema, N. M., & Stenzel, O. J. (2014). Dust deflation by dust devils on Mars derived from optical depth measurements using the shadow method in HiRISE images. *Planetary and Space Science*, *93*, 54–64. <https://doi.org/10.1016/j.pss.2014.01.016>
- Reiss, D., Spiga, A., & Erkeling, G. (2014). The horizontal motion of dust devils on Mars derived from CRISM and CTX/HiRISE observations. *Icarus*, *227*, 8–20. <https://doi.org/10.1016/j.icarus.2013.08.028>
- Rennó, N. O., Burkett, M. L., & Larkin, M. P. (1998). A simple thermodynamical theory for dust devils. *Journal of the Atmospheric Sciences*, *55*(21), 3244–3252. [https://doi.org/10.1175/1520-0469\(1998\)055<3244:ASTTFD>2.0.CO;2](https://doi.org/10.1175/1520-0469(1998)055<3244:ASTTFD>2.0.CO;2)
- Rodríguez-Manfredi, J. A., & de la Torre Juárez, M. (2021). Mars 2020 perseverance rover Mars environmental dynamics analyzer (MEDA) experiment data record (EDR) and reduced data record (RDR) data products archive bundle. *PDS Atmospheres Node*, *10*, 1522849.
- Rodríguez-Manfredi, J. A., De la Torre Juárez, M., Alonso, A., Apéstigue, V., Arruego, I., Atienza, T., et al. (2021). The Mars environmental dynamics analyzer, meda. A suite of environmental sensors for the Mars 2020 mission. *Space Science Reviews*, *217*(3), 1–86.
- Spiga, A., Murdoch, N., Lorenz, R., Forget, F., Newman, C., Rodríguez, S., et al. (2021). A study of daytime convective vortices and turbulence in the Martian planetary boundary layer based on half-a-year of insight atmospheric measurements and large-eddy simulations. *Journal of Geophysical Research: Planets*, *126*(1), e2020JE006511. <https://doi.org/10.1029/2020je006511>
- Stanzel, C., Pätzold, M., Williams, D. A., Whelley, P. L., Greeley, R., Neukum, G., et al. (2008). Dust devil speeds, directions of motion and general characteristics observed by the Mars express high resolution stereo camera. *Icarus*, *197*(1), 39–51. <https://doi.org/10.1016/j.icarus.2008.04.017>
- Steakley, K., & Murphy, J. (2016). A year of convective vortex activity at gale crater. *Icarus*, *278*, 180–193. <https://doi.org/10.1016/j.icarus.2016.06.010>
- Sullivan, R., & Kok, J. (2017). Aeolian saltation on Mars at low wind speeds. *Journal of Geophysical Research: Planets*, *122*(10), 2111–2143. <https://doi.org/10.1002/2017je005275>
- Thomas, P., & Gierasch, P. J. (1985). Dust devils on Mars. *Science*, *230*(4722), 175–177. <https://doi.org/10.1126/science.230.4722.175>
- Toigo, A. D., Richardson, M. I., Ewald, S. P., & Gierasch, P. J. (2003). Numerical simulation of Martian dust devils. *Journal of Geophysical Research*, *108*(E6), 5047. <https://doi.org/10.1029/2002je002002>

- Toledo, D. (2022). Perseverance MEDA-RDS: Radiative transfer data and dust devil retrievals. *Zenodo*. <https://doi.org/10.5281/zenodo.7441253>
- Toledo, D., Arruego, I., Apéstigue, V., Jiménez, J., Gómez, L., Yela, M., et al. (2017). Measurement of dust optical depth using the solar irradiance sensor (SIS) onboard the exomars 2016 EDM. *Planetary and Space Science*, *138*, 33–43. <https://doi.org/10.1016/j.pss.2017.01.015>
- Toledo, D., Rannou, P., Pommereau, J.-P., Sarkissian, A., & Foujols, T. (2016). Measurement of aerosol optical depth and sub-visual cloud detection using the optical depth sensor (ODS). *Atmospheric Measurement Techniques*, *9*(2), 455–467. <https://doi.org/10.5194/amt-9-455-2016>
- Towner, M. (2009). Characteristics of large Martian dust devils using Mars odyssey thermal emission imaging system visual and infrared images. *Journal of Geophysical Research*, *114*(E2), E02010. <https://doi.org/10.1029/2008je003220>
- Waller, D. (2011). *Active dust devils on mars: A comparison of six spacecraft landing sites*. Arizona State University.
- Wang, Y., Li, B., Zhang, J., Ling, Z., Qiao, L., Chen, S., & Qu, S. (2021). The preliminary study of dust devil tracks in southern utopia planitia, landing area of tianwen-1 mission. *Remote Sensing*, *13*(13), 2601. <https://doi.org/10.3390/rs13132601>
- Whelley, P. L., & Greeley, R. (2008). The distribution of dust devil activity on Mars. *Journal of Geophysical Research*, *113*(E7), E07002. <https://doi.org/10.1029/2007je002966>
- Wolff, M., Smith, M., Clancy, R., Arvidson, R., Kahre, M., Seelos IV, F., et al. (2009). Wavelength dependence of dust aerosol single scattering albedo as observed by the compact reconnaissance imaging spectrometer. *Journal of Geophysical Research*, *114*(E2), E00D04. <https://doi.org/10.1029/2009je003350>
- Wolff, M. J., Clancy, R. T., Goguen, J. D., Malin, M. C., & Cantor, B. A. (2010). Ultraviolet dust aerosol properties as observed by marci. *Icarus*, *208*(1), 143–155. <https://doi.org/10.1016/j.icarus.2010.01.010>
- Zurek, R. W., Barnes, J. R., Haberle, R. M., Pollack, J. B., Tillman, J. E., & Leovy, C. B. (1992). Dynamics of the atmosphere of Mars. *MARS*, 835–933. <https://doi.org/10.2307/j.ctt207g59v.30>